EXPLORATORY INVESTIGATIONS OF THE EFFECTS OF GAS INJECTION THROUGH A POROUS MODEL ON SEPARATION, TRANSITION, STATIC STABILITY AND CONTROL EFFECTIVENESS OF A BLUNT ENTRY BODY AT MACH NUMBER 7.3

by

Mark V. Morkovin and John C. Donohoe

July 1967

NASA-CR-73121

Prepared Under Contract No. NAS-2-3873 by

MARTIN MARIETTA CORPORATION

Baltimore, Maryland 21203

for

NATIONAL AERONAUTICS AND SPACE ADMINISTRATION

EXPLORATORY INVESTIGATIONS OF THE EFFECTS OF GAS INJECTION THROUGH A POROUS MODEL ON SEPARATION, TRANSITION, STATIC STABILITY AND CONTROL EFFECTIVENESS OF A BLUNT RE-ENTRY BODY AT MACH NUMBER 7.3

by

Mark V. Morkovin and John C. Donohoe

SUMMARY

An exploratory research program to determine the effects of gaseous injection from the wall of a blunted entry body has been completed. Wind tunnel tests were made in the NASA 3.5-foot Hypersonic Wind Tunnel at Mach 7.3 and a nominal Reynolds number (based on length) of 0.48 million, using a porous stainless steel model. By metering room and low temperature nitrogen through the permeable model shell, model wall-to-stagnation temperature ratios from 0.08 to 0.35 were achieved. The mass rate parameter, $\dot{m}$ (ratio of injected mass to the product of free stream velocity, density and body base area), was varied from zero to 0.05. The location of separation and transition was judged from extensive spark shadowgraphs and from measurements of pressures, temperature and heat flux rates at the surface of the porous model just upstream of the 1.6 aspect ratio trailing edge flap.

For zero flap deflection, the effect of wall blowing on the external aerodynamics was found to be very much smaller than on sharp-nose bodies of comparable base area. For finite flap deflections, the separation pocket and associated force fields seem to be governed by the lateral venting of the pocket at the base of the flap, by the magnitude of the favorable pressure gradient upstream of the flap, and by the backpressure due to the flap. The effect of mass injection and cooling play a secondary role, especially at higher angles of attack. Similarly, the onset of large-scale instability of the separated pocket when the flap protrudes sufficiently through the bow shock wave is not hastened nor aggravated by the mass injection.

INTRODUCTION

Current maneuverable entry bodies are thermally protected with heat shields which burn and pyrolyze, giving off gases which add to the total mass of the boundary layer surrounding the vehicle. The consequent variable displacement of the outer flow field brings about an incremental variable pressure field and modification of the static stability of the vehicle. In addition, the presence of the low-speed ablation gases within the considerably thickened boundary layer may affect critical separation regions that occur upstream of any aerodynamic controls. Any consequent loss or reduction of control could be severely detrimental to vehicle performance. The key characteristic is the susceptibility of the boundary layer to separation with increasing mass injection in the presence of a rise in pressure caused by a fixed flap deflection. For sharp cones, the constancy of pressure along rays from the apex may well facilitate boundary layer separation all the way from the nose for sufficiently high rise in backpressure because of the low inertia of the injected mass near the wall. The situation is not expected to be catastrophic for maneuverable bodies which generally have (or can be modified to have) a favorable pressure gradient immediately upstream of the flaps. This pressure field accelerates the low-inertia gases near the wall and helps limit the size of the essentially unavoidable separated pocket of laminar flow.

No criteria for separation in presence of gaseous emanation from the wall, comparable to those based on the free-interaction concepts of Chapman, Kuehn and Larson (ref. 1), have appeared in the literature. In fact, no systematic study leading to similar criteria for the practically important cases of separation in presence of pressure gradients without mass injection at the wall appeared to have been made.

Therefore, this investigation aimed at exploring the sensitivity of the separation phenomena, under simulated conditions of practical interest, to changes in mass addition, pressure gradient (angle of attack), backpressure (flap deflection) and (to a lesser extent) wall temperature. Since the separation characteristics play an important role in the potentially destructive unsteady oscillations of the separated pocket when the flap deflections are large (ref. 2) a limited check of the effect of mass injection on the unsteadiness was also made.

The pioneering experience of Chapman, et al.(ref. 1) made it clear that visualization of the boundary layer behavior is essential in exploratory studies of separation. Consequently, most of the experiments were performed at the relatively high free stream stagnation pressure of 40.8×10^4 kg/sq m and at the relatively low Mach number of 7.3, for which the shadow technique registered the separation with little

ambiguity. However, as in reference 1, transition of the separated layer, thickened by injection, to a turbulent one proved to be an important complicating factor.

With minor exceptions, the visualization and the rest of the measurements are fully consistent and provide a qualitative understanding of the different complex subphenomena at play in the present experiments. It is believed that these qualitative observations have more general validity which can be usefully applied to other Mach and Reynolds numbers and other geometrical configurations. In particular, the present experiments can serve as ground work for more definitive basic studies of separation in the presence of mass injection on simpler geometries on one hand, and for more applied investigations of specific entry vehicles on the other.

SYMBOLS

C_A	axial force coefficient, $\frac{F_X}{qS}$
C_m	pitching moment coefficient, $\frac{M_Y}{qS\ell}$
C_N	normal force coefficient, $\frac{F_Z}{qS}$
F_X	force along X-axis
F_Z	force along Z-axis
ℓ	length of model (see fig. 1)
M	Mach number
M_Y	pitching moment (see fig. 1 for moment center)
$\dot{m}$	ratio of mass rate of injection to product of free stream velocity, free stream density and body base area
p	static pressure
p_{t_1}	tunnel stagnation pressure
p_{t_2}	stagnation pressure down stream of a normal shock
p_{w_1}	forward model surface pressure
p_{w_2}	mid model surface pressure
p_{w_3}	aft model surface pressure
q	dynamic pressure
$\dot{q}$	heat transfer rate at the wall
$\dot{q}_{st}$	stagnation point heat transfer rate
R	Reynolds number

S	model base area
T	absolute temperature
T_{w_1}	forward model surface temperature
T_{w_2}	aft model surface temperature
u	velocity component parallel to the wall
v	velocity component normal to the wall
V	magnitude of velocity
x	distance from nose of model measured along the X axis
α	angle of attack (see fig. 1)
δ	boundary layer thickness; flap-deflection angle
δ^*	displacement thickness of boundary layer
μ	viscosity coefficient
ρ	gas density

Subscripts:

e	outer edge of the attached or separated layer
t	total conditions
w	wall

APPARATUS AND TEST METHODS

Wind Tunnel

The NASA-Ames Research Center 3.5-foot Hypersonic Wind Tunnel is a blowdown facility equipped with three interchangeable nozzles contoured for Mach numbers of 5, 7 and 10. Experiments made as part of this research program used the Mach 7 nozzle that produced a Mach 7.3 stream and which was operated at a Reynolds number per meter of approximately 4.9 million (R/ft of 1.5 million) and at total temperatures of 833° K and 1083° K (1500° and 1950° R). Running times for the selected tunnel operating conditions were in excess of two minutes.

The model was mounted on a support sting which was secured to a movable strut in the tunnel quick-insert mechanism. This provided a means for isolating the model outside the tunnel during starting transients and while changing angle of attack. Data were obtained during two to four quick immersions into the airstream at angles of attack from 0 to 20 degrees.

Model

Figure 1 gives a description of the model shape used in these experiments. It had a blunt nose, rounded top and sides, and a flat lower surface ahead of an 1.6 aspect ratio trailing flap. It was intended to have typical features of a shaped maneuverable entry vehicle as contrasted with missiles which are usually axisymmetric and without flaps. Surface pressure and heat rate distributions over the undeflected flap configuration were available from other programs, which made interpretation of results of this investigation more reliable.

A 0.00635-meter thick porous stainless steel shell, constructed by Mott Metallurgical Corporation, formed the basic model. This shell was attached to a solid stainless steel aft bulkhead using a silicon rubber seal; the bulkhead provided the structure for mounting the model to a strain gage balance as well as an attachment for the solid steel trailing flap. The aft end of the model was sealed with Teflon O rings capable of withstanding the cold nitrogen injectant as well as the high tunnel stagnation temperature. Flap angles of 0, 20, 30 and 40 degrees were manufactured for the model and an additional 60-degree flap was made during the test by mounting a 20-degree wedge on the original 40-degree flap.

The strain gage balance was too long to be protected from the airstream by the model itself. Therefore, it was enclosed with a split sleeve that was clamped to the sting. As shown in figure 1, interlocking

parts minimized the crossflow across the balance at the model base. Gaseous nitrogen was supplied to the model plenum through two 0.00635-meter outside diameter insulated tubes that were connected to the model by means of nickel bellows. Figure 2 shows the complete installation on the tunnel quick-insert system.

The porous model shell was manufactured from 316 stainless steel powder that had been passed through a number 325 sieve (smallest opening 44 microns). The material had approximately 37 percent open volume as determined by weighing known geometric samples. Caution had to be exercised during the test to keep the model shell below a temperature of approximately 420° C. This restriction was based on possible changes in porosity if the particles of metal were to oxidize and thus fill up the voids. Model wall temperature was monitored during the program and the quick-insert strut had to be withdrawn from the tunnel during several of the runs to protect the model shell. The porous body appeared to suffer only minor pitting from the tunnel airstream and sampling of the flow rate distribution over the surface upon completion of the three weeks of testing showed no significant blocking of the pores.

The model shell as received from the manufacturer required smoothing of the surface to remove irregularities. This was accomplished by using emery paper which thoroughly closed the outside surface of the model. Porosity was restored by etching the shell and flushing it out with detergent. Following this, a calibration was made to check the uniformity of permeability of the model nose. Figure 3 presents values of mass flow rate obtained by connecting a 0.0127 meter inside diameter surgical rubber tube to a small flow meter and placing it against the model surface at selected locations ahead of the trailing flap. The average deviation from the mean flow rate was within ± 9 percent.

Figure 4 presents an outline of the gas flow system prepared by NASA* for this program. High pressure nitrogen was throttled through a series of valves, passed through a flow meter, and passed either through or around a LN_2 cooled heat exchanger and on into the model. The large pressure drop through the porous model skin permitted easy control and measurement of the mass flow rate at relatively high pressure during the test. This large model skin pressure drop (14,000 to 20,000 kg/sq m) minimized "bleeding" of tunnel flow through the model from a region of high pressure (such as the model nose) to regions of lower pressure. It is also minimized differential mass flow rates over the model surface as a result of local pressure gradients.

---

*The efficient design was conceived by H. K. Larson and J. B. McDevitt of Ames Research Center.

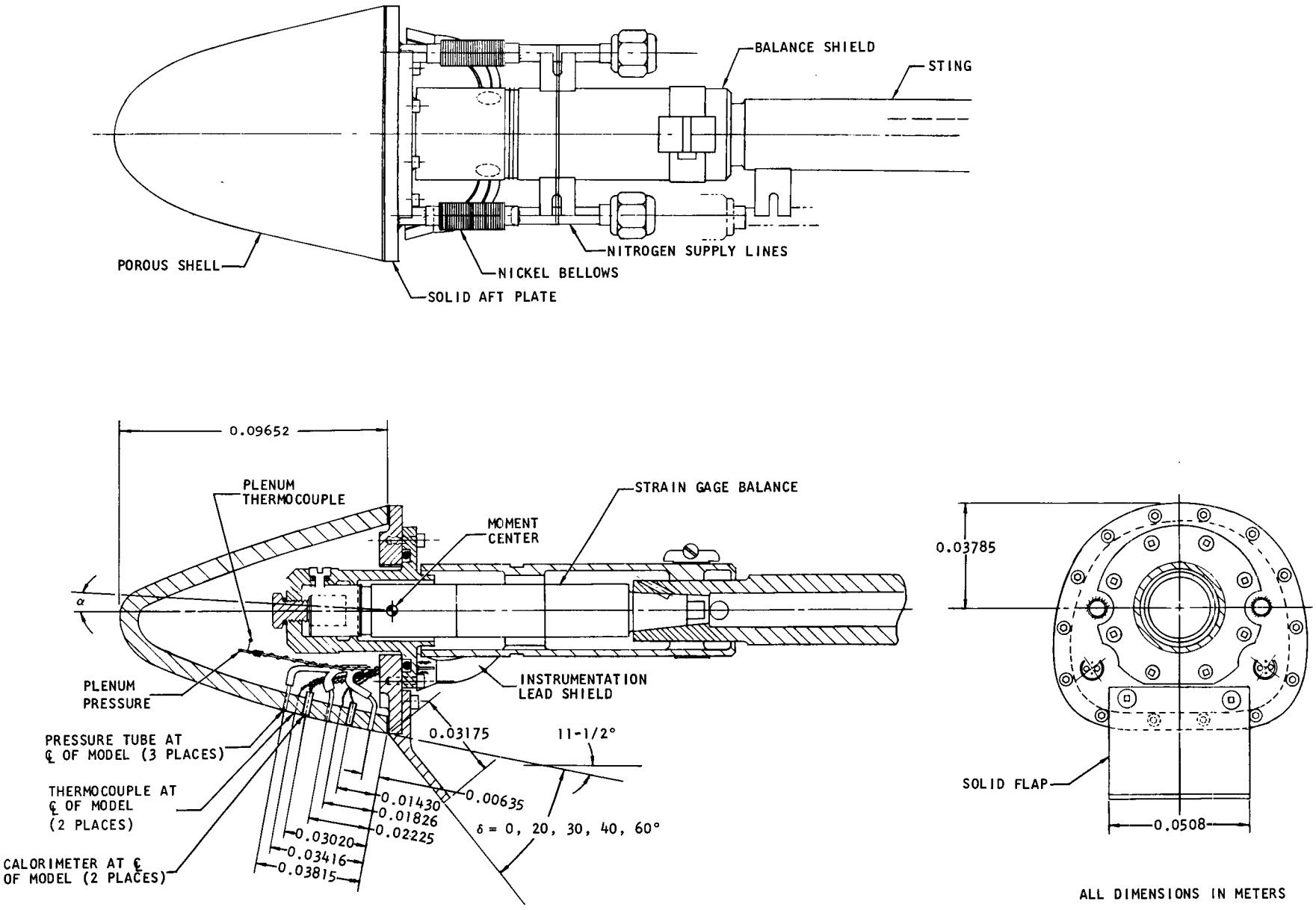

FIGURE 1. MODEL DESCRIPTION

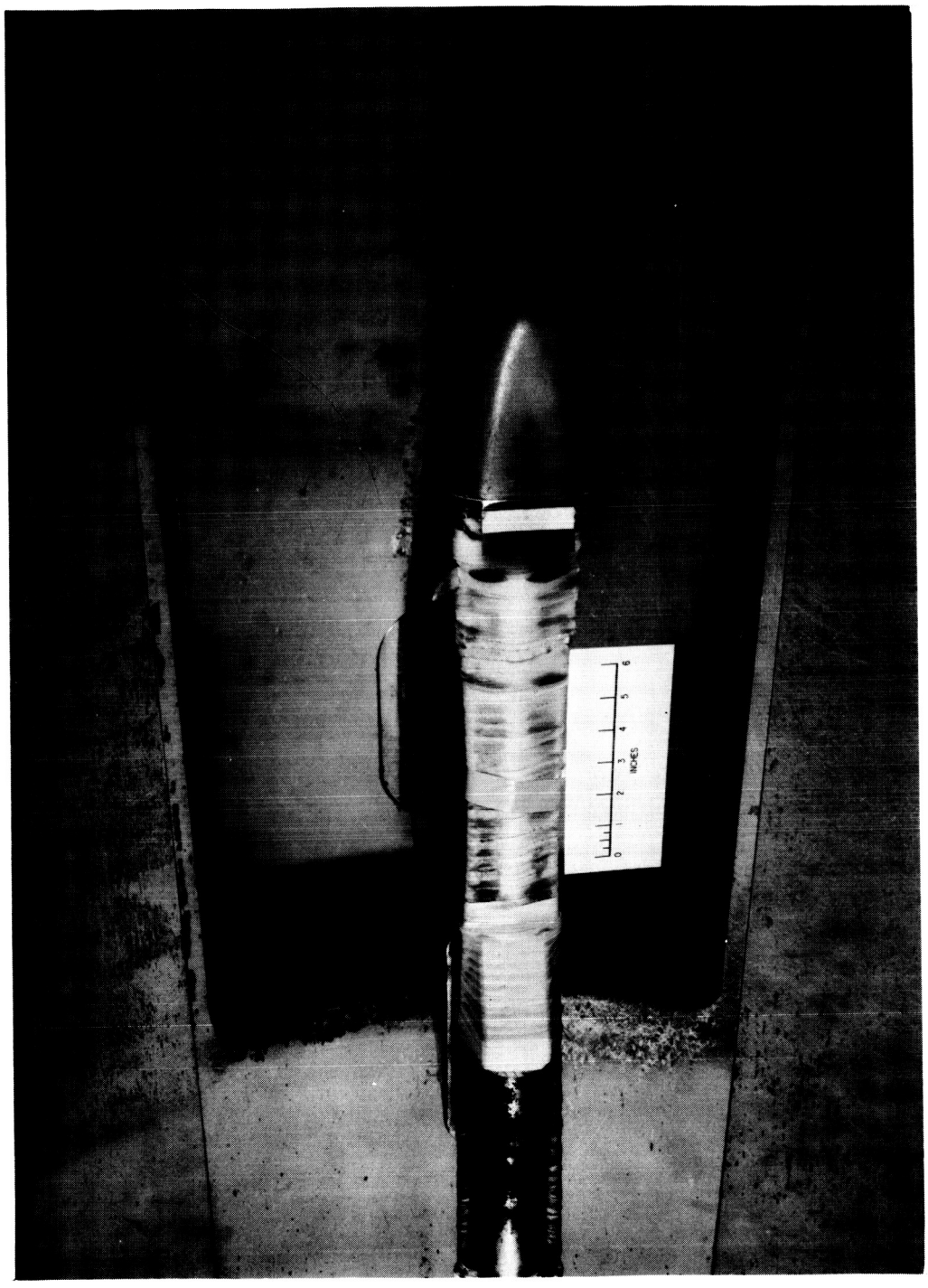

FIGURE 2. MODEL INSTALLED IN 3.5-FOOT TUNNEL

X/ℓ	B_{LEFT}	A_{LEFT}	℄	A_{RIGHT}	B_{RIGHT}
	← (KG/SEC)/SQ M →				
0.247	0.119	0.124	0.130	0.128	0.116
0.411	0.105	0.116	0.128	0.124	0.112
0.576	0.105	0.116	0.124	0.112	0.109
0.740	0.112	0.145	0.141	0.128	0.130
0.905	0.128	0.153	0.145	0.145	0.141

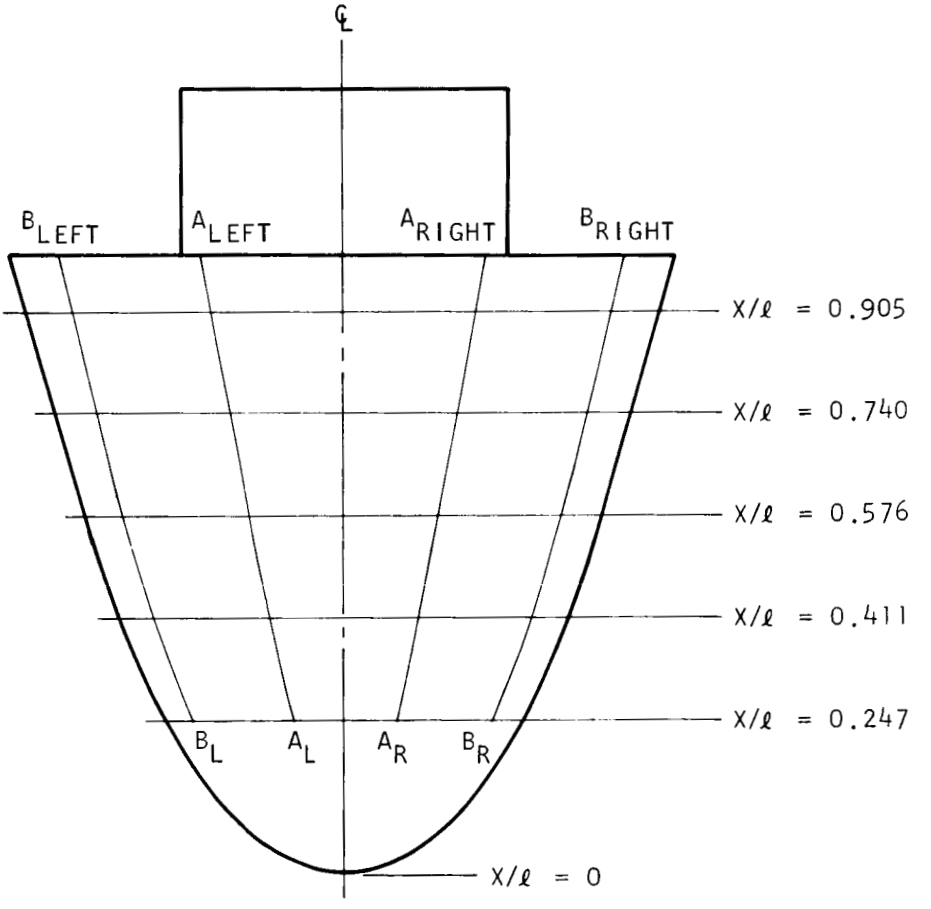

BOTTOM VIEW

FIGURE 3. MODEL FLOW RATE DISTRIBUTION

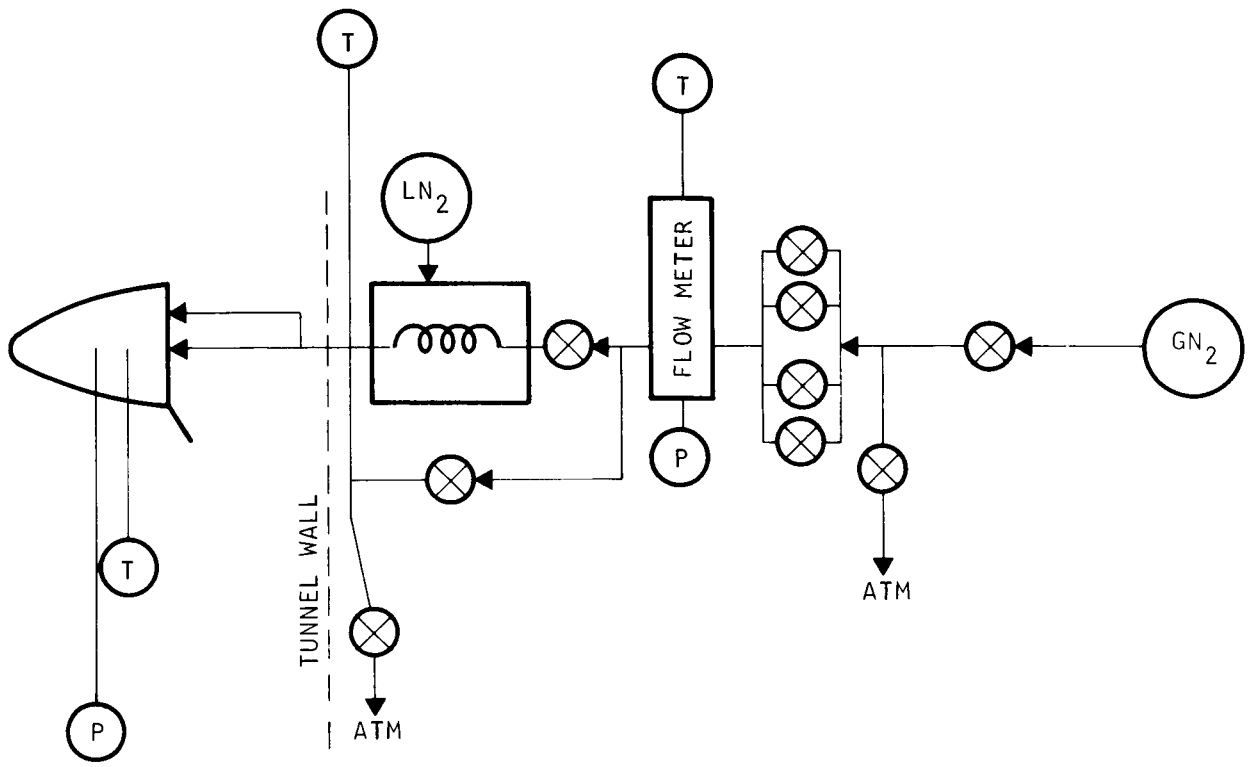

FIGURE 4. GAS FLOW SYSTEM

Instrumentation

The model was mounted on a six-component strain gage balance using two small nickel bellows to minimize the tare of the gas supply lines. As shown in figure 1, the lower centerline ahead of the flap was instrumented with three static pressure orifices, two outside wall thermocouples and two calorimeters. The design of the calorimeters is shown in figure 5. The pressure orifices were made from 0.001194 meter inside diameter Monel tubing which was potted into a hole drilled in the porous shell. The calorimeters and chromel-constantan thermocouples were also attached in place with a bead of epoxy on the inside of the shell. This, in effect, created a very small plug in the skin which is surrounded by the permeable metal.

All data were recorded on magnetic tape every 0.06 second from a time just before insertion into the airstream until the model was withdrawn. A photograph of the flowmeter and its pressure was obtained once during each model insert.

Optical Techniques

Illumination for the shadowgraph system, the main optical tool used throughout the experiments, was furnished by a spark source of 0.6 to 0.7 microsecond duration. The light rays traveled 3.66 meters to the centerline of the tunnel and another 1.26 meters after grazing the surface of the model before reaching the photographic film, resulting in a nominal magnification of 1.37. Helpful examples of construction of angular deviations of light rays passing through laminar and turbulent boundary layers for which the density was least at the wall can be found in references 3 and 4.

In the present experiments, the entropy layer due to the detached shock wave kept the local boundary layer edge static temperature, T_e, above 47 percent of the total temperature, T_t. With the range of the ratio of wall-to-total temperature between 0.1 and 0.35, the static temperature through the boundary layer was increasing and, therefore, the density was decreasing from the wall outward. Ray construction, such as those of references 3 and 4, demonstrate that, for a constant density gradient, the light passing through the boundary layer would simply bend into the normal body shadow. Figure 6, at the standard conditions of the bulk of the experiments (T_t = 1083° K and $p_t = 40.8 \times 10^4$ kg/sq m), shows that the condition $(\rho_w - \rho_e)/\rho_w \approx 0.4$ just prior to separation does not produce sufficient contrast for the profiles without mass injection to distinguish between the normal diffraction patterns and a slightly darker

band expected at the outer edge of the layer where the gradient tends to disappear. Nevertheless, these standard conditions were adopted because a lower Reynolds number was desired, and because fair visual discrimination was brought about by even small mass injection rates, which thickened the layer and twisted the density profile to provide more contrast (see fig. 7 for $\dot{m}$ = 0.009 and fig. 16b for $\dot{m}$ = 0.005). The reader will notice from figures 8 and 9 that, even for zero injection, the shadowgraphs at higher angles of attack provide substantial information.

Use of spark illumination rather than longer exposures made it necessary to replace the visual criteria of transition of references 1 and 3 with those of references 5 and 6; that is, direct identification of large eddies, "hairiness" of the image of turbulent boundary layer, and radiation of irregular Mach waves from the eddies. Actually, because of the unavoidably large distance from the model to the plane of the film, the large eddies could be seen only infrequently, for instance in the instability of the slip surface issuing from the intersection of the flap shock with the bow wave in figure 9. Instead, the scattering of light by the first eddies would simply obliterate the regular white-dark bands corresponding to the laminar layer, making identification of the instantaneous position of transition generally quite positive, such as in figures 8 and 10 (see also figs. 16b and 17b). In figure 8, the identification is corroborated by the irregular radiated sound waves from the large eddies of the separated transiting layer. The diagnosis of transition upstream of separation (occurring only at highest blowing) in figure 10 was supported by the temperature and heat transfer variations at the wall, with which the information from the shadowgraphs was always checked. The criterion of "hairiness" (sic ref. 6) or graininess had to be applied with caution because the splotchiness due to minute pitting of the windows, and light scattering by chips in the window near the model nose tended to give false indications. Thus, the graininess in the appearance of the edge of the body in figure 8 upstream of the separation has nothing to do with turbulence because the separated layer is clearly laminar. When cold nitrogen was injected, however, the density gradients increased by a factor of approximately three, and there was no question about the hairiness (as in figure 11 just upstream of the flap) being caused by turbulence.

The black-white band, seemingly issuing from within the body in figure 11 illustrates the magnitude of image displacements which can be incurred in case of large density gradients. Even smaller displacements for the body at room temperature cause some uncertainty in the identification of the other important characteristic--the forward separation edge of the layer. For instance, in figure 8, the clearly identifiable shocklet caused by the separation does not extrapolate (even with due attention to smaller Mach numbers near the wall) to the point from

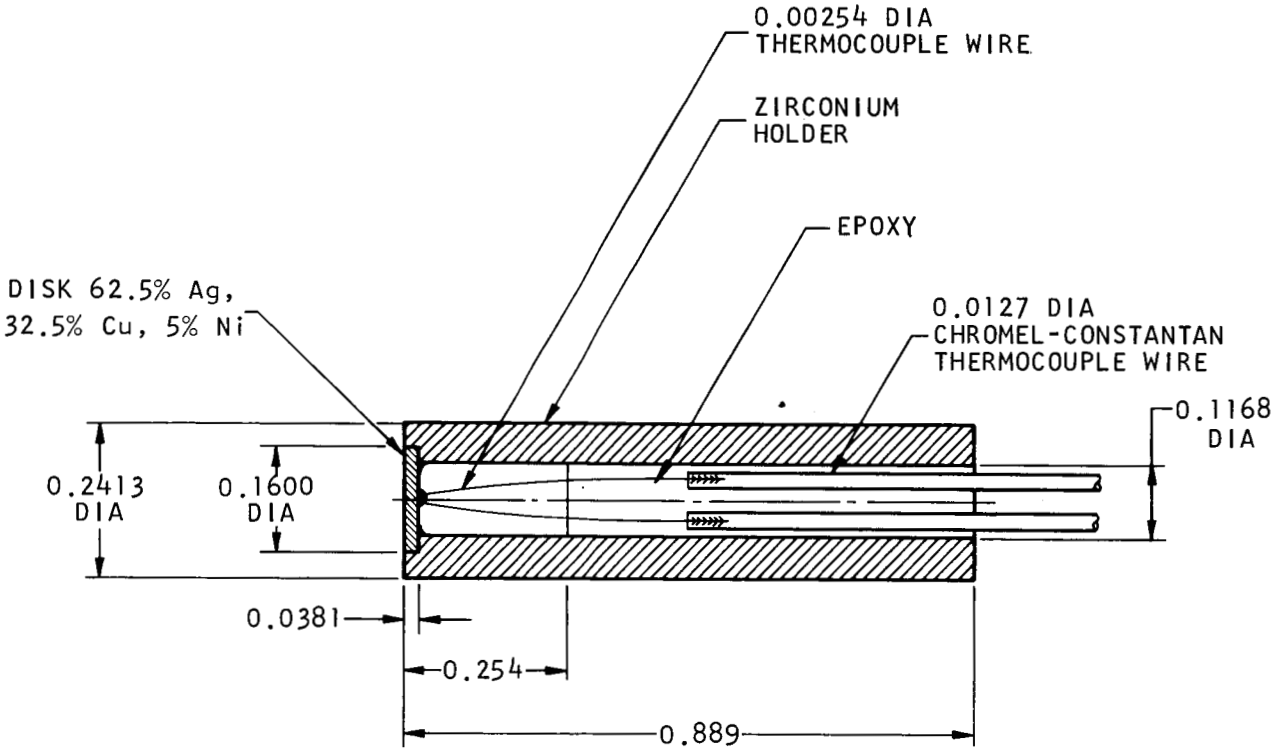

FIGURE 5. CALORIMETER DESIGN

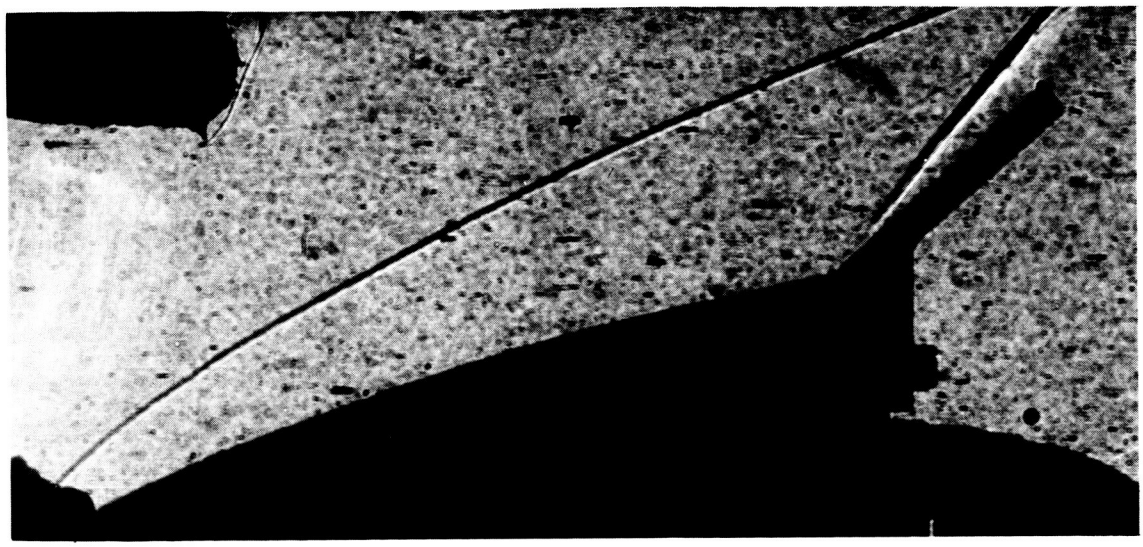

FIGURE 6. SHADOWGRAPH: $\alpha = 0°$, $\delta = 30°$, $\dot{m} = 0$, $T_{w_1}/T_t = 0.34$

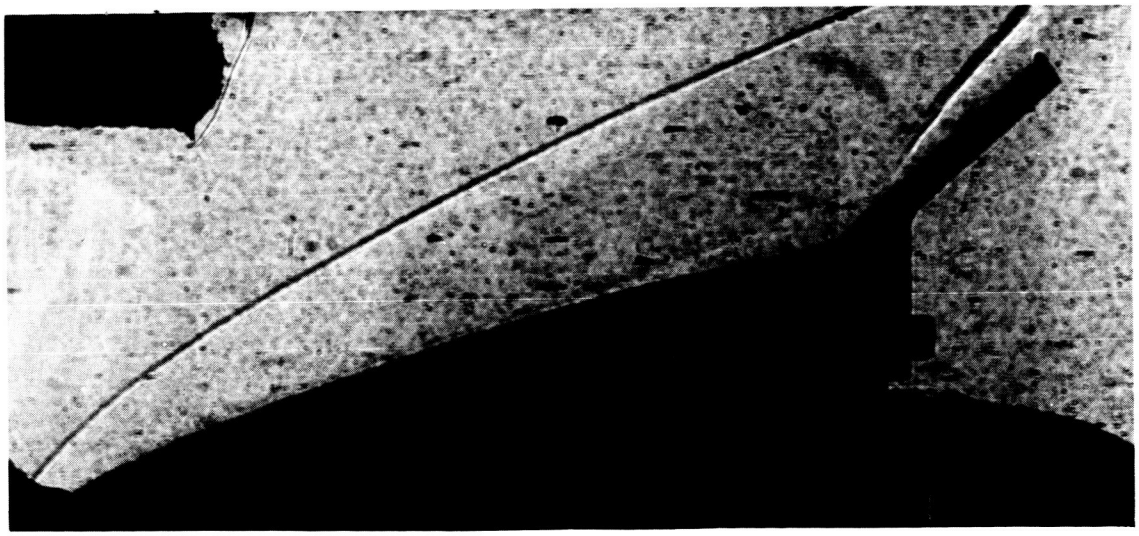

FIGURE 7. SHADOWGRAPH: $\alpha = 0°$, $\delta = 30°$, $\dot{m} = 0.009$, $T_{w_1}/T_t = 0.31$

which the laminar separated layer seemingly originates. In figure 9, the discrepancy can be resolved only if one extrapolates the two lines into the interior of the body, which is probably correct but which can still lead to an unassessable error.

With a few exceptions of malfunctioning, one to five shadowgraphs were available for the analysis of each test condition. These were processed with the above criteria for transition and separation and checked for consistency with the pressure and heat transfer information. An admittedly subjective estimate for the probable spread of these locations was also made (fig. 18) based on the details of each sample.

Visualization of Separated Pocket Shape

The danger of contaminating the pores of the sintered steel shell prevented the use of the surface oil film technique for delineation of the separated pocket over the body (e.g., ref. 1). A combination of color-changing temperature sensitive paints and a series of paints melting at temperatures from 56° to 389° C were used for assessing the areas of backward and forward flow and areas of high heating over the solid steel flap at several mass injection rates and $\alpha = 0°$, $\delta = 30°$.* By watching the flap through a window with a prefocused transit theodolite, the melting and flowing of the various paint dots could be observed as it developed after insertion of the model into the hot stream. These visual impressions, combined with a photographic record of the painted flap after each run, were amalgamated with information from the set of corresponding shadowgraphs and are presented in figures 16 and 17 and are discussed later.

*The helpful guidance of H. L. Seegmiller is acknowledged.

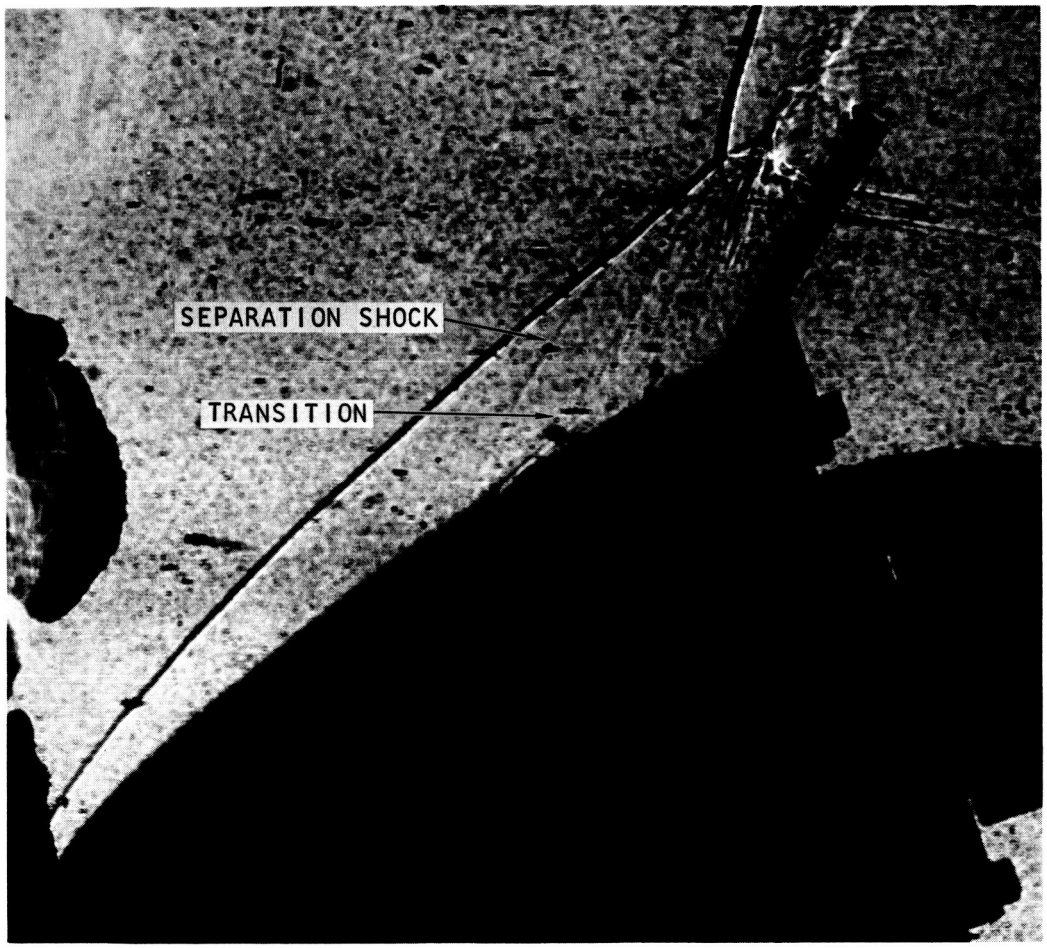

FIGURE 8. SHADOWGRAPH: $\alpha = 20°$, $\delta = 30°$, $\dot{m} = 0$, $T_{w_1}/T_t = 0.34$

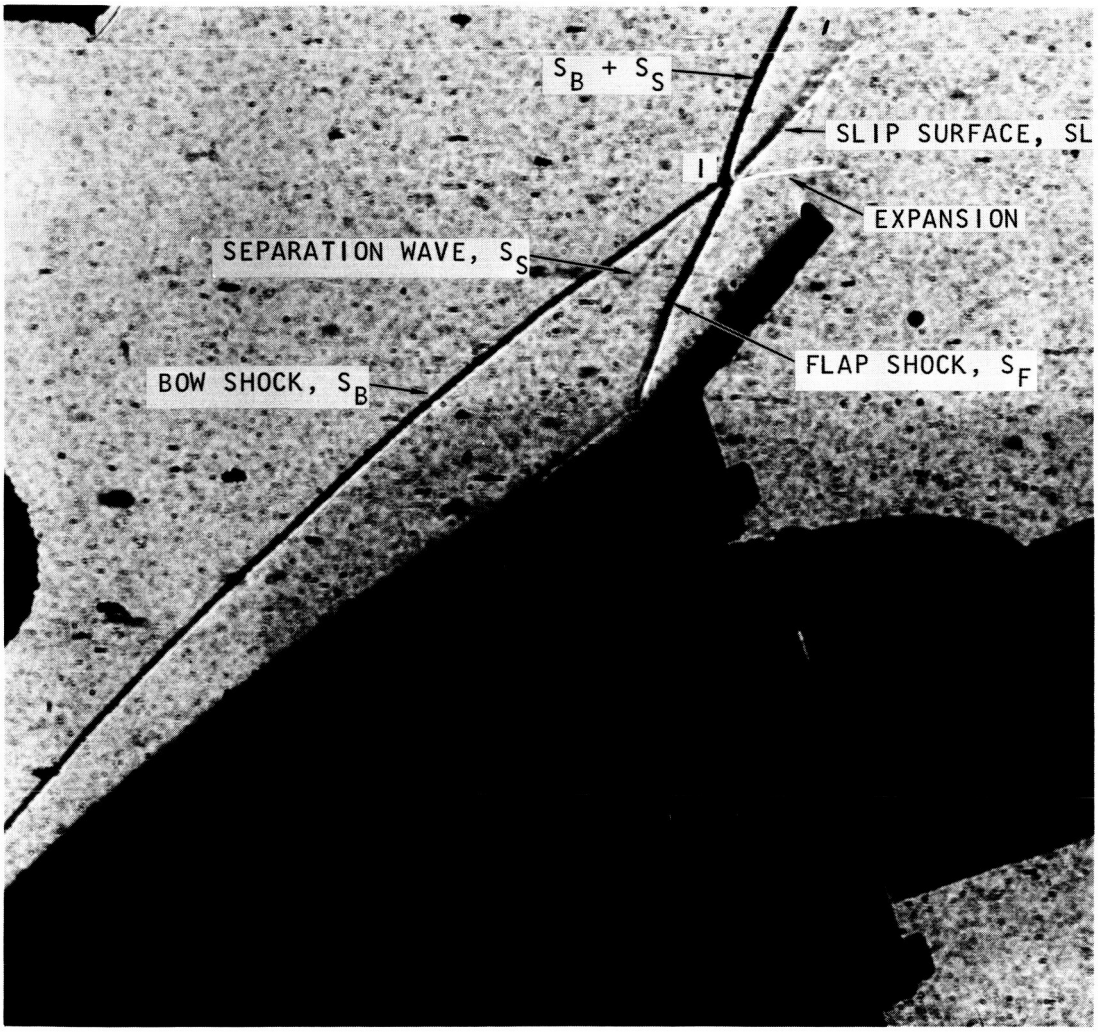

FIGURE 9. SHADOWGRAPH: $\alpha = 20°$, $\delta = 20°$, $m = 0°$, $T_{w_1}/T_t = 0.31$

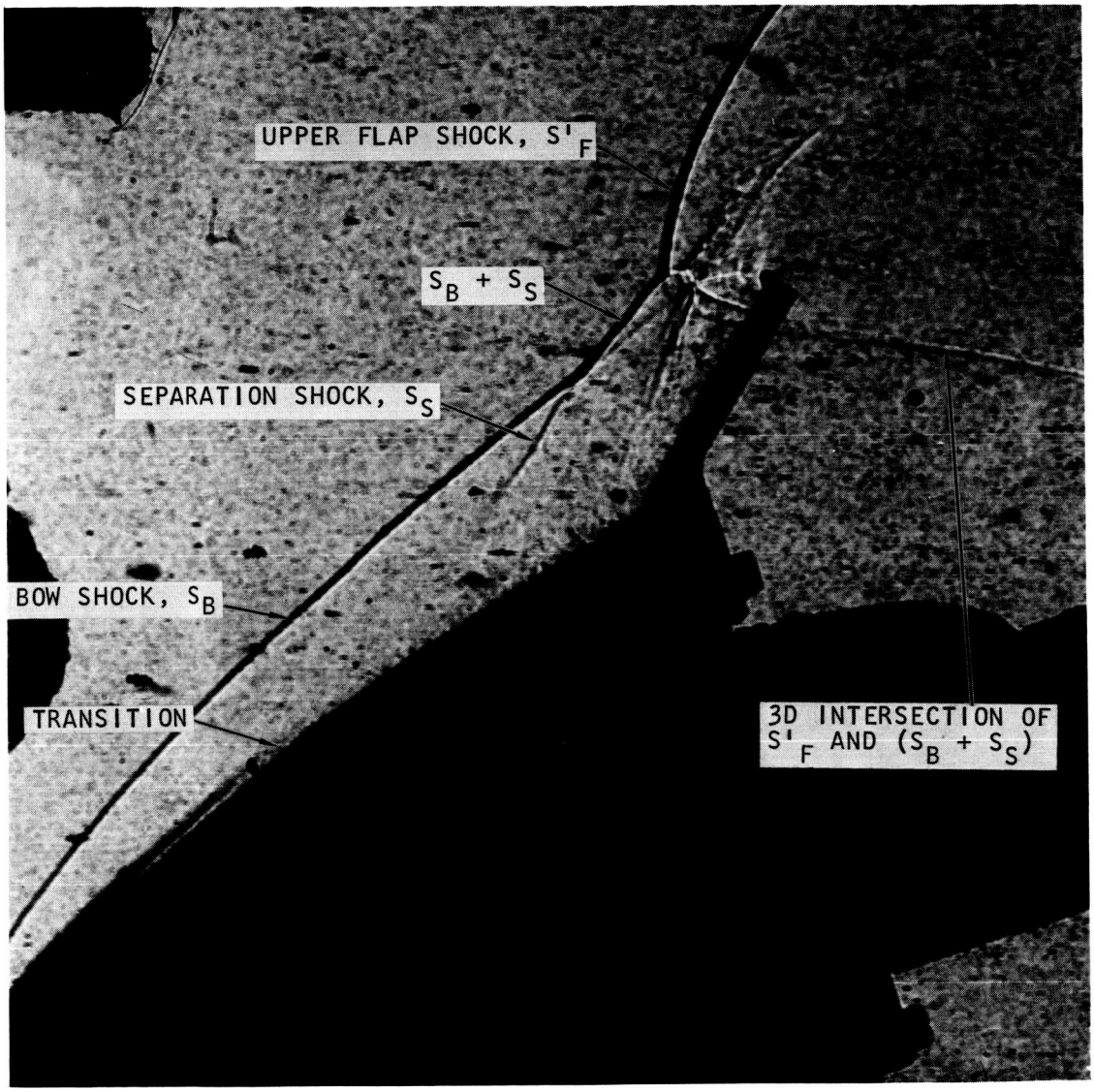

FIGURE 10. SHADOWGRAPH: $\alpha = 20°$, $\delta = 30°$, $\mathscr{M} = 0.046$, $T_{w_1}/T_t = 0.32$

FIGURE 11. SHADOWGRAPH: $\alpha = 0°$, $\delta = 30°$, $\dot{m} = 0.046$, $T_{w_1}/T_t = 0.10$

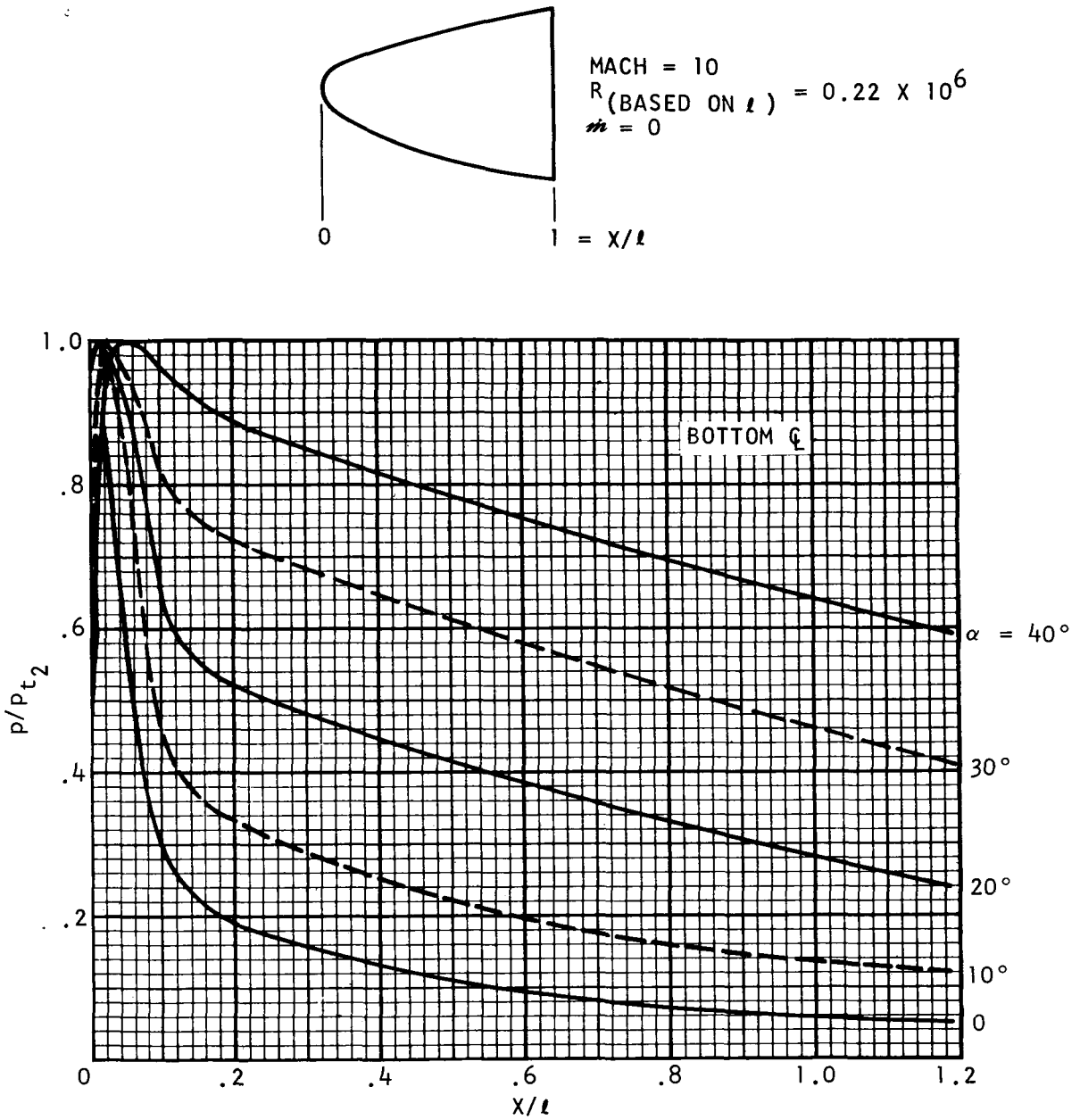

FIGURE 12. VARIATION OF PRESSURE RATIO WITH STATION--NO FLAP DEFLECTION

DATA REDUCTION AND ACCURACY

Force data were reduced using the balance axis system shown in figure 1 with the pitching moment center located on the balance centerline, 0.09652 meters aft of the model nose. The reference length (ℓ) was also 0.09652 meters, and the reference area (S) was 0.006516 square meters (the model base area). Since tests were preformed in a blowdown facility, the dynamic pressure was computed from tunnel conditions recorded simultaneously with basic force data.

Surface pressure measurements obtained at three locations ahead of the flap were nondimensionalized by dividing by a calculated stagnation pressure downstream of a normal shock (p_{t_2}), accounting for caloric imperfections due to high tunnel total temperature using reference 7.* Figure 12 shows a distribution of pressure ratio over the nose with no flap deflection and no mass addition. These data have been cross plotted in figure 13 versus angle of attack at the stations instrumented with pressure orifices. Present test data for zero mass injection (runs 15 and 48) have been plotted on figure 13, and show good agreement with hypersonic solid-model data previously obtained.

Heat rate measurements were obtained at two locations on the model centerline ahead of the flap using small calorimeters (fig. 5). These instruments were calibrated by mounting them in a sample of sintered stainless steel, duplicating the environment in the model, and then exposing the gage disk to a calibrated propane-air torch. The resulting calibration factor was combined with histories of gage disk temperature versus time taken for the first 0.20 second after the model reached the tunnel centerline. The measured model heat rate was ratioed to the stagnation heat rate ($\dot{q}_{st}$) calculated from the Fay and Riddell equations for a spherical nose (ref. 8) using a Lewis number of one, a Prandtl number of 0.71, and a model nose radius of 0.01905 meters.** The model wall temperature used for calculation of $\dot{q}_{st}$ was the gage

---

*Values of p_{t_2} were calculated for each angle of attack using measured tunnel conditions. Typical values for the nominal tunnel total temperature 833° K and 1083° K cases were 2.9×10^3 and 4.9×10^3 kg/sq m, respectively.

**Values of $\dot{q}_{st}$ were calculated for each angle of attack using measured tunnel conditions. Nominal values for tunnel total temperatures of 833° K and 1083° K were 218×10^3 and 440×10^3 J/sq m-sec, respectively (19.2 and 38.8 Btu/sq ft-sec).

temperature recorded just prior to insertion in the tunnel flow. Figure 14 presents a distribution of heat rate ratio ($\dot{q}/\dot{q}_{st}$) over the nose with no flap deflection on a non porous body. The data have been cross plotted in figure 15 at model stations instrumented with the two calorimeters. Comparison of test data from this program (runs 10, 15 and 48) shows good agreement with data obtained at Mach number 10 on a thin skinned model.

It is difficult to assess the many errors in measurement of the pressures, temperatures and heat flux when these gages are embedded in the porous material and thus disturb the local mass and heat flow. Any estimates would be more on expression of hope than of probable fact. Nevertheless, the agreement of the inferred local heat flux and pressure with data from nonporous models (figs. 13 and 15) was encouraging. Excellent consistency of the many overlapping measurements, varying with different parameters, tends to endow the results in the presence of the gaseous injection with substantial credibility.

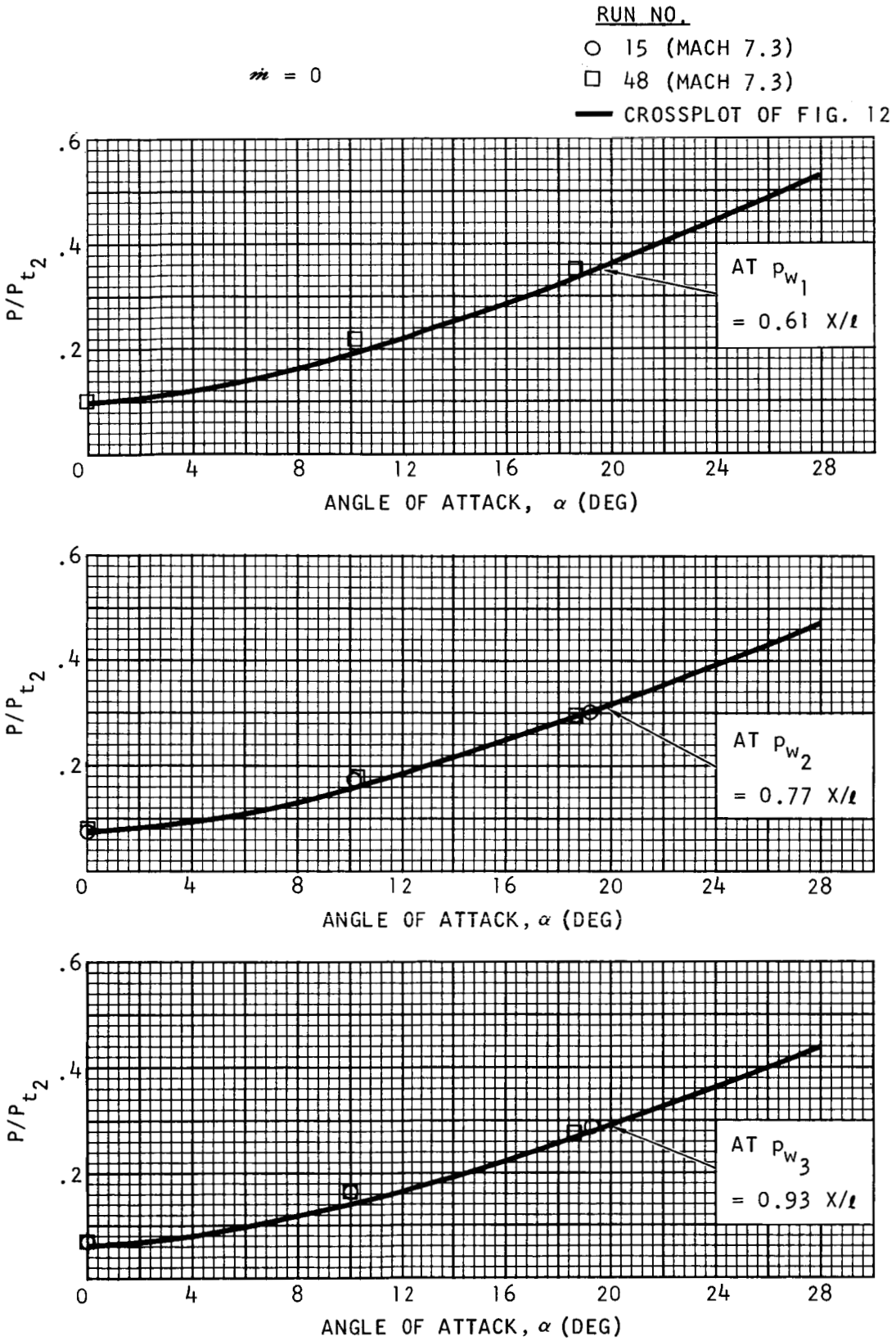

FIGURE 13. VARIATION OF PRESSURE RATIO WITH ANGLE OF ATTACK AT INSTRUMENTED STATIONS--NO FLAP DEFLECTION

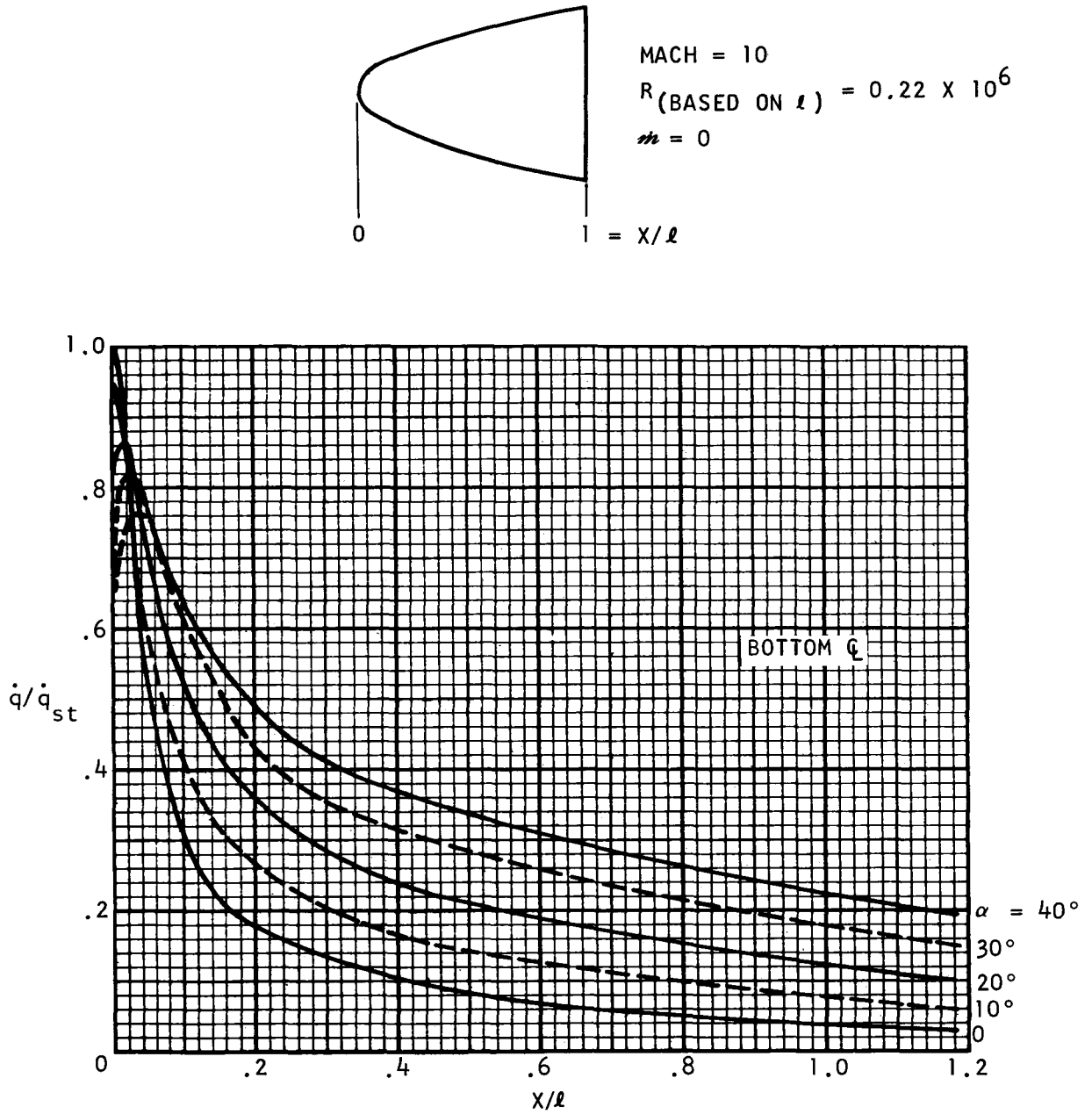

FIGURE 14. VARIATION OF HEAT RATE RATIO WITH STATION--NO FLAP DEFLECTION

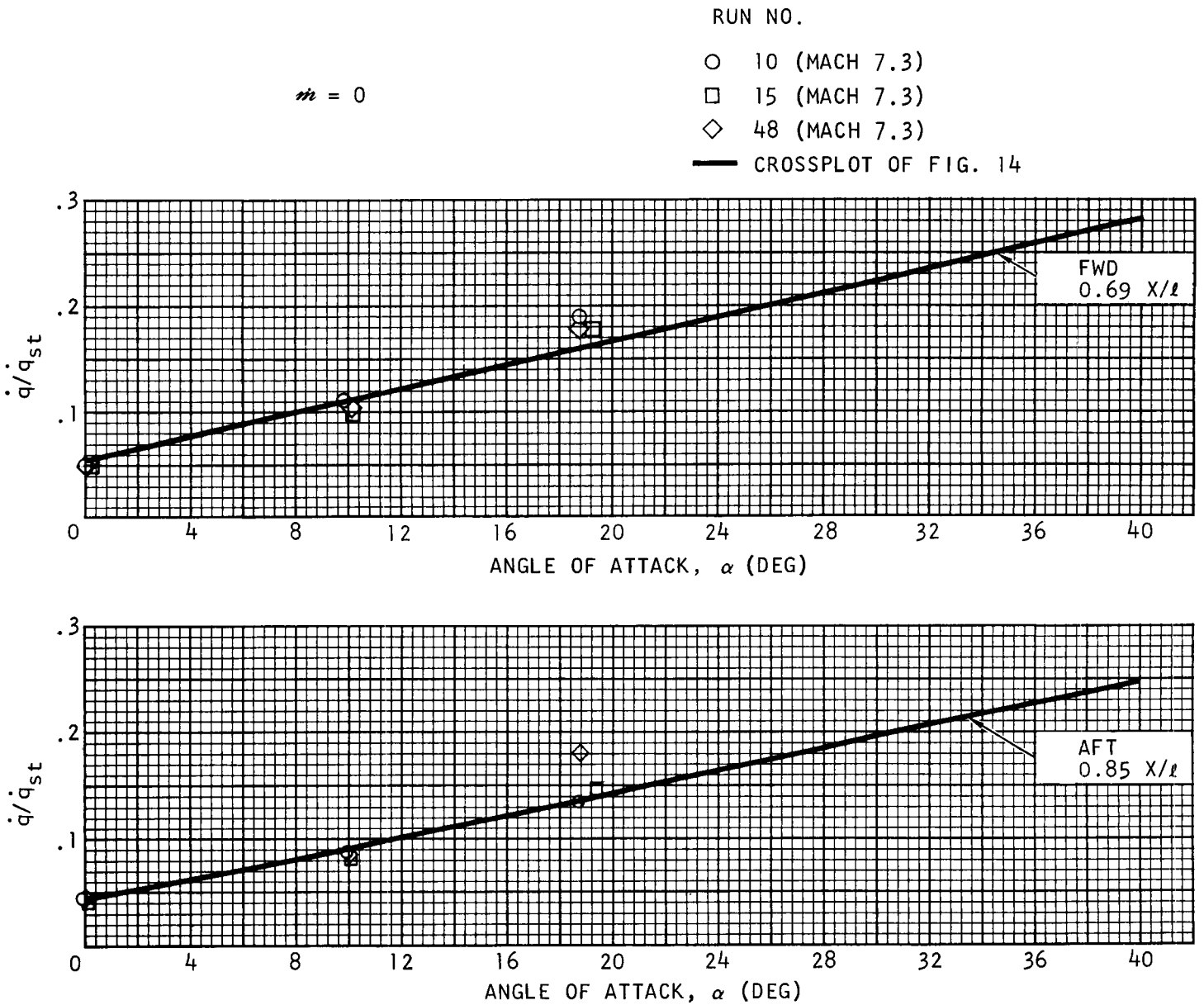

FIGURE 15. VARIATION OF HEAT RATE RATIO WITH ANGLE OF ATTACK AT INSTRUMENTED STATIONS--NO FLAP DEFLECTION

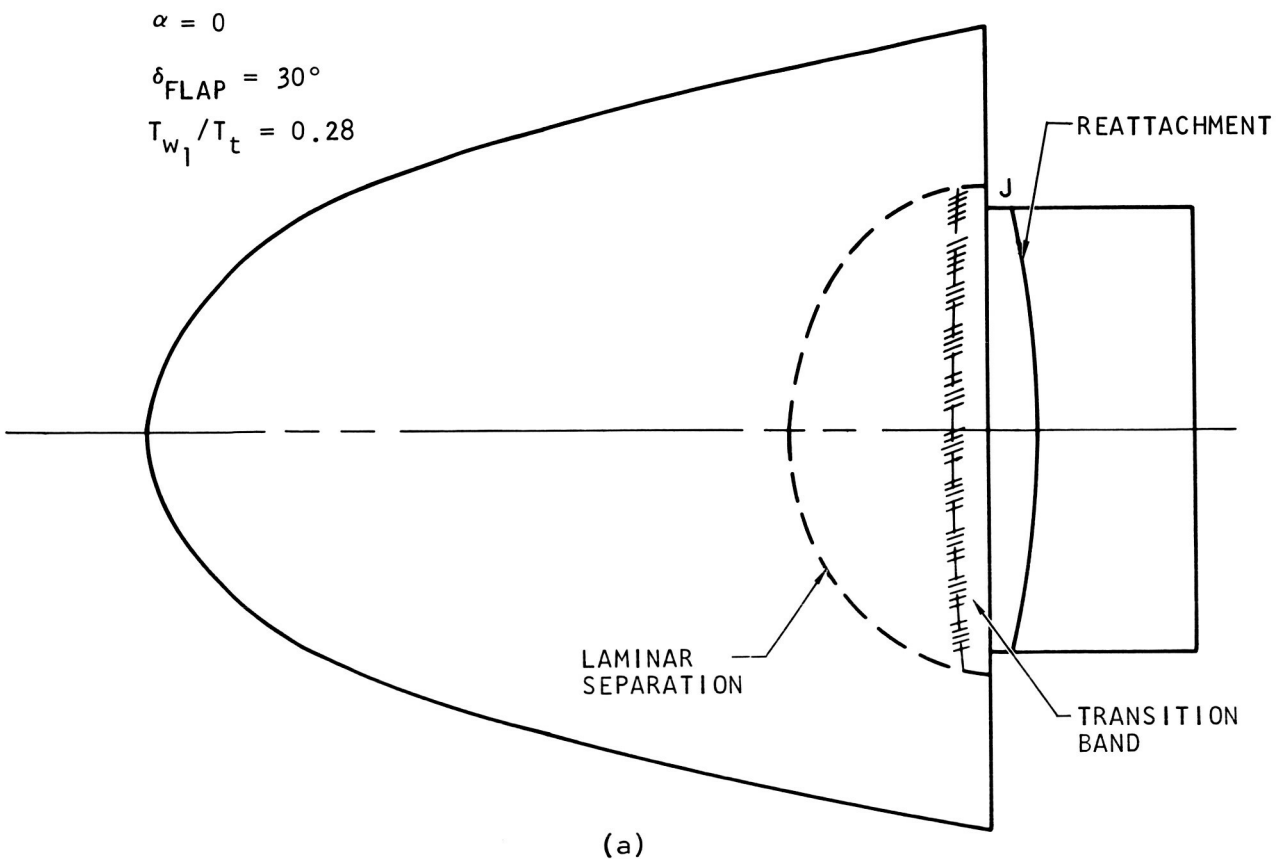

(a)

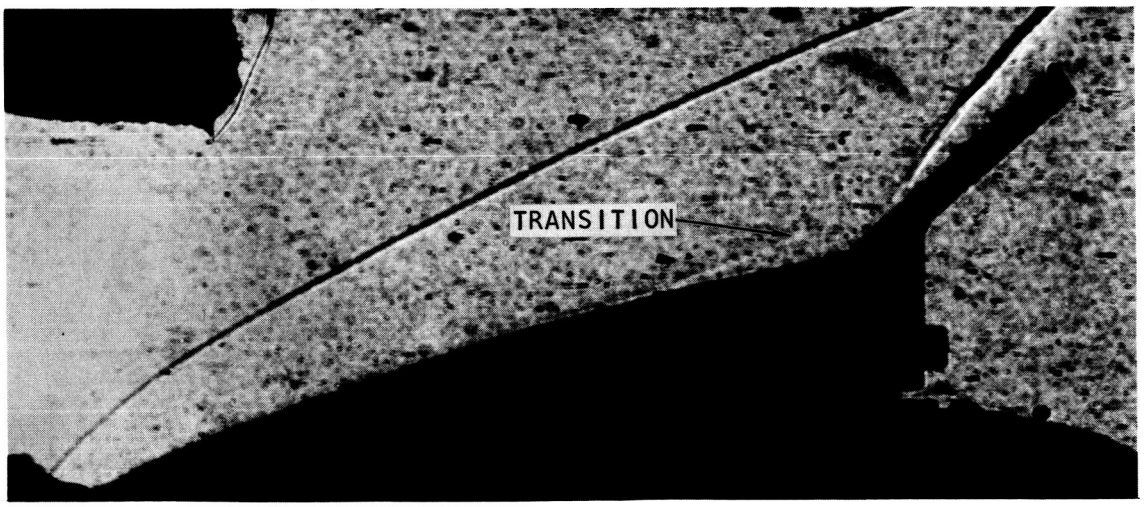

(b)

FIGURE 16. SHAPE AND SIZE OF SEPARATED POCKET FOR $\dot{m}$ = 0.005

RESULTS AND DISCUSSION

Size and Shape of Separated Pocket and Consequences

According to the Closing Panel Discussion of the 1966 AGARD Symposium on Separated Flow (ref. 9), the location and closure of separated pockets represents one of the unsolved fluid-mechanical problems, even for two-dimensional laminar flows without wall injection. In addition to various mathematical difficulties, the main responsibility for this gap in our knowledge rests on the physical coupling between the pressure field (external to the boundary layers and separated pocket) and the occurrence of the separation and reattachment lines. Changes in this pressure field affect the changes in stability and control characteristics of interest herein.

As an aid to interpretation, the composite results of the shadowgraph and thermal paint information on the three-dimensional shape and size of the pocket for zero angle of attack and 30 degree flap deflection are presented in figures 16 and 17 for the extreme cases of blowing tested. The salient departure from the more academic (nonsolved) two-dimensional cases is caused by the presence of powerful "sinks" at the junctures, J, of the side edges of the flap and the trailing edge of the body. The mass flux, which is turned back into the pocket by the strong adverse pressure gradient at reattachment, can now move laterally and discharge through two vortical funnels at J. One consequence of this side motion is to keep the reattachment line on the flap closer to the hinge line, causing higher pressures over a larger area of the flap with obvious influences on forces, moments and heat transfer.

Since paint or other tracers could not be used on the model itself for fear of contaminating the pores, the inferred lateral spreading over the body itself (figs. 16a and 17a) was based on previous first-hand experience (ref. 10). Actually, there is little leeway in the admissible plan view of the separation bubbles once the leading edge of the separation and the reattachment line are experimentally established, except perhaps for the possible near discontinuity of slope at the line of transition from laminar to turbulent layer (observed in profile view), at least for moderate blowing rates, say $\mathscr{m} \leq 0.02$.

For these moderate injection rates, the separation pockets are nearly maximal in size at zero angle of attack, presumably because the pressure gradient in front of the flap is the mildest so that a given backpressure can "climb" farther upstream on the pressure curve in figure 12. However, for small and moderate blowing rates at a given δ, an increase in α can cause a sufficiently larger backpressure so that pockets grow slightly larger than that shown in figure 16a. As the angle of attack was increased

to 10° and 20° for the 30° flap angle, the leading edge of separation stabilized at about 0.03556 m (1.4 in.) upstream of the hinge line, almost independently of the blowing rates from zero to 0.02. Apparently, as backpressures increase, so do the lateral pressure gradients, and the lateral mass outflow limits the upstream separation.

In the case of high blowing ($\dot{m}$ of 0.031 and 0.046 to 0.05), the separation pocket decreased in length as angle of attack increased, so that at $\alpha = 20°$, $\delta = 30°$, the length corresponding to that in figure 17a decreased from 0.05334 m (2.1 in.) to approximately 0.03181 m (1.25 in.), with transition preceding the separation by approximately 0.01782 m (0.7 in.). Whether this decrease was due primarily to the turbulence at the separation line, which invariably shortens separated pockets, or to the inevitably increased cross-flow out of the pocket as the angle of attack rises, is not clear. Still, the upstream extent of the pocket differs little at $\alpha = 20°$, $\delta = 30°$ for all the blowing rates, including zero and 0.05, despite the fact that only the latter exhibited turbulent separation. It is perhaps noteworthy in this context, that the body pressures under these separated pockets did not differ by more than 10 percent for these various injection conditions at $\alpha = 20°$, $\delta = 30°$. Unfortunately, the experimental conditions did not allow including pressures over the flap, where significant differences should be expected, judging from shadowgraphs such as shown in figures 8 and 10.

From a comparison of the top and middle rows of figures 18a through 18d, it would appear that, with the exception of the more extreme blowing rates, $\dot{m}$ has little influence on the separation criteria discussed in the Introduction, in spite of the fact that it must influence strongly enough the local skin friction; i.e., the measure of the "sticking" characteristic of the boundary layer of Chapman et al.(ref. 1). It would seem that the pressure gradients become the dominant factor with respect to separation, an observation well worth exploring in some future, more basic experiments.

One should inquire at this stage about the probable changes in blowing rates across the separation line in actual flight of an ablating body. In purely laminar separated pockets, the local heat transfer rates generally drop 30 to 50 percent below the corresponding laminar nonseparated rates (ref. 11), but generally rise above them underneath those parts of the pocket where the separated layer has become turbulent. In addition, various chemical rates for the given material enter the picture so that occasionally higher rates of ablation and/or erosion are observed in separated regions. Unfortunately, attempts to block the injection in an area under the separation bubble like that in figure 17a were unsuccessful; short of spoiling the porous shell. However, lack of sensitivity of the leading separation line to blowing rates up to 0.02 (and possibly beyond) lead one to expect that the departure in these experiments from some possible "actual ablator behavior in separated pockets" would have

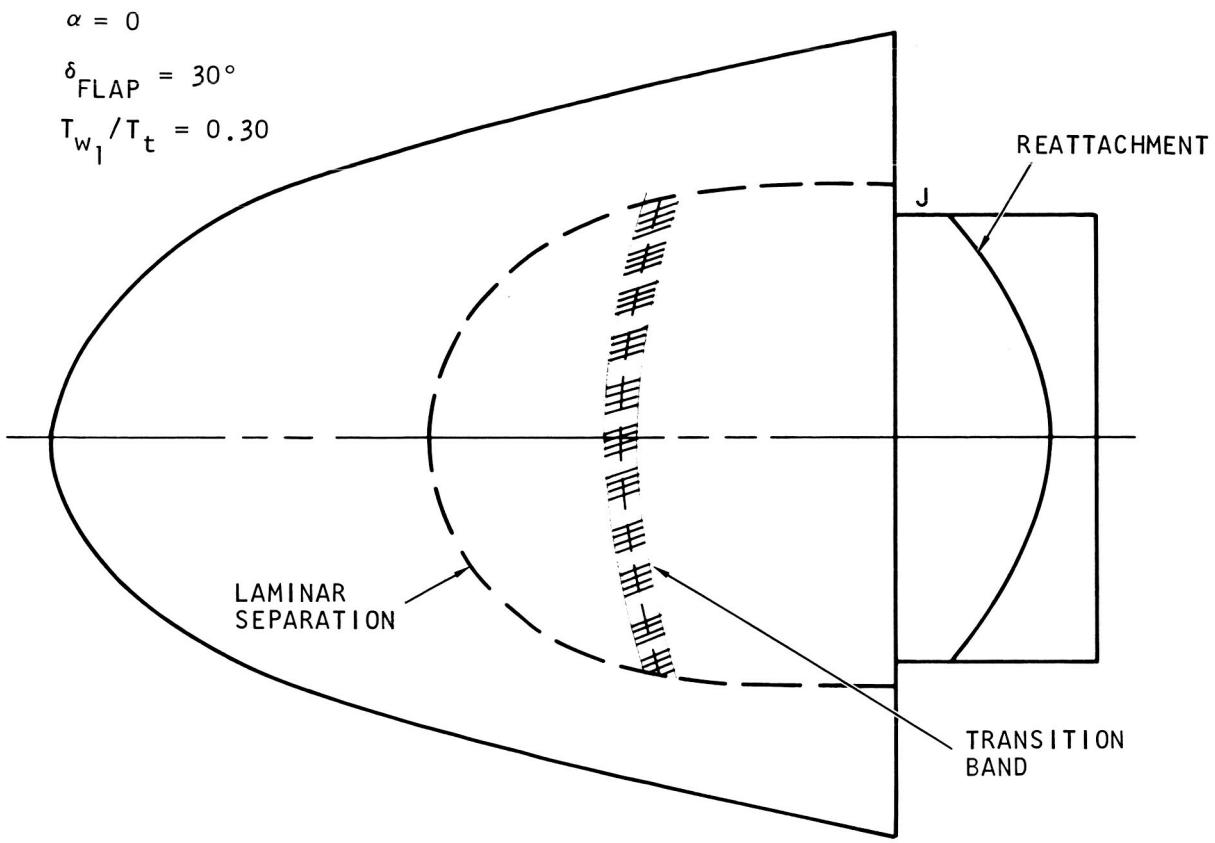

(a)

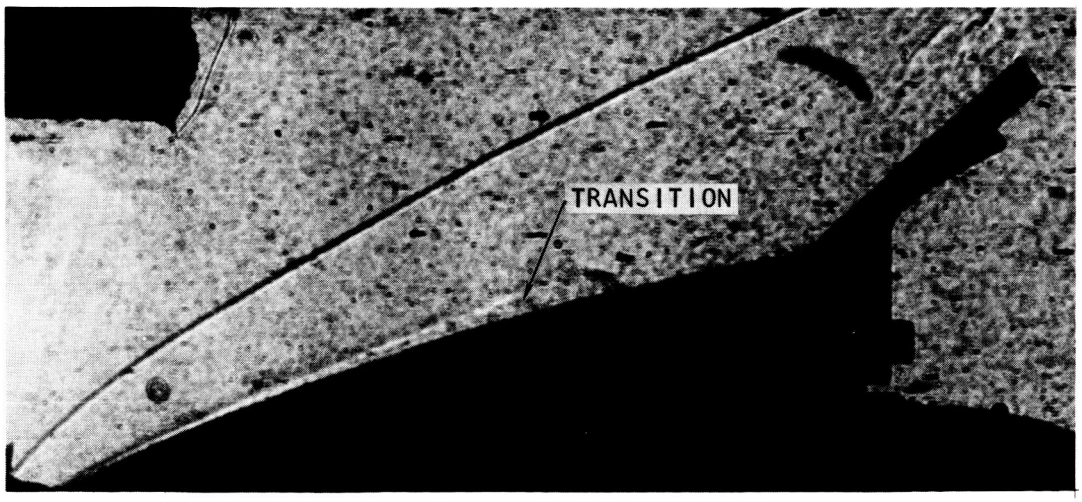

(b)

FIGURE 17. SHAPE AND SIZE OF SEPARATED POCKET FOR $\dot{m}$ = 0.046

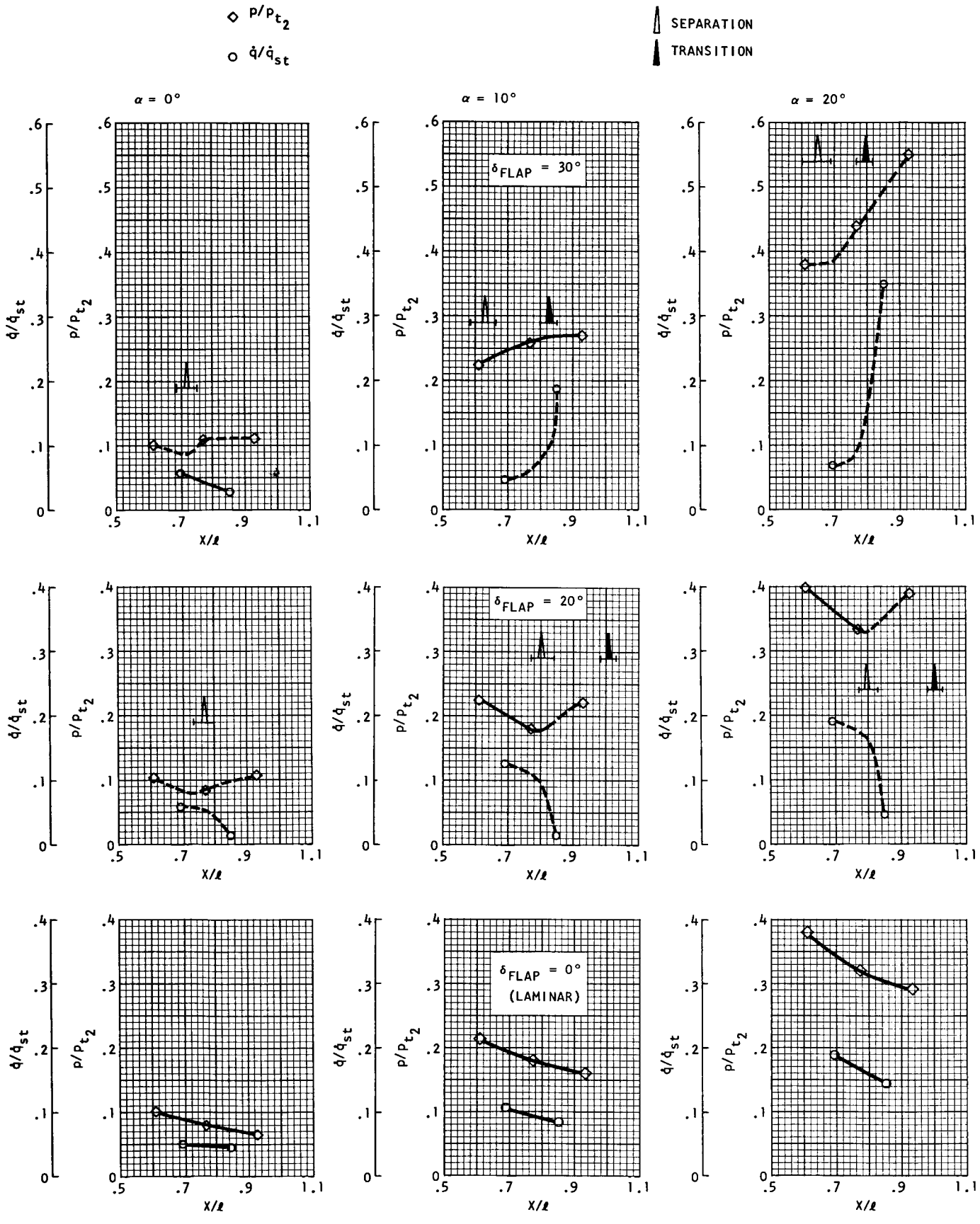

a) m = 0

FIGURE 18. PRESSURE AND HEAT RATES AHEAD OF THE FLAP: MACH 7.3

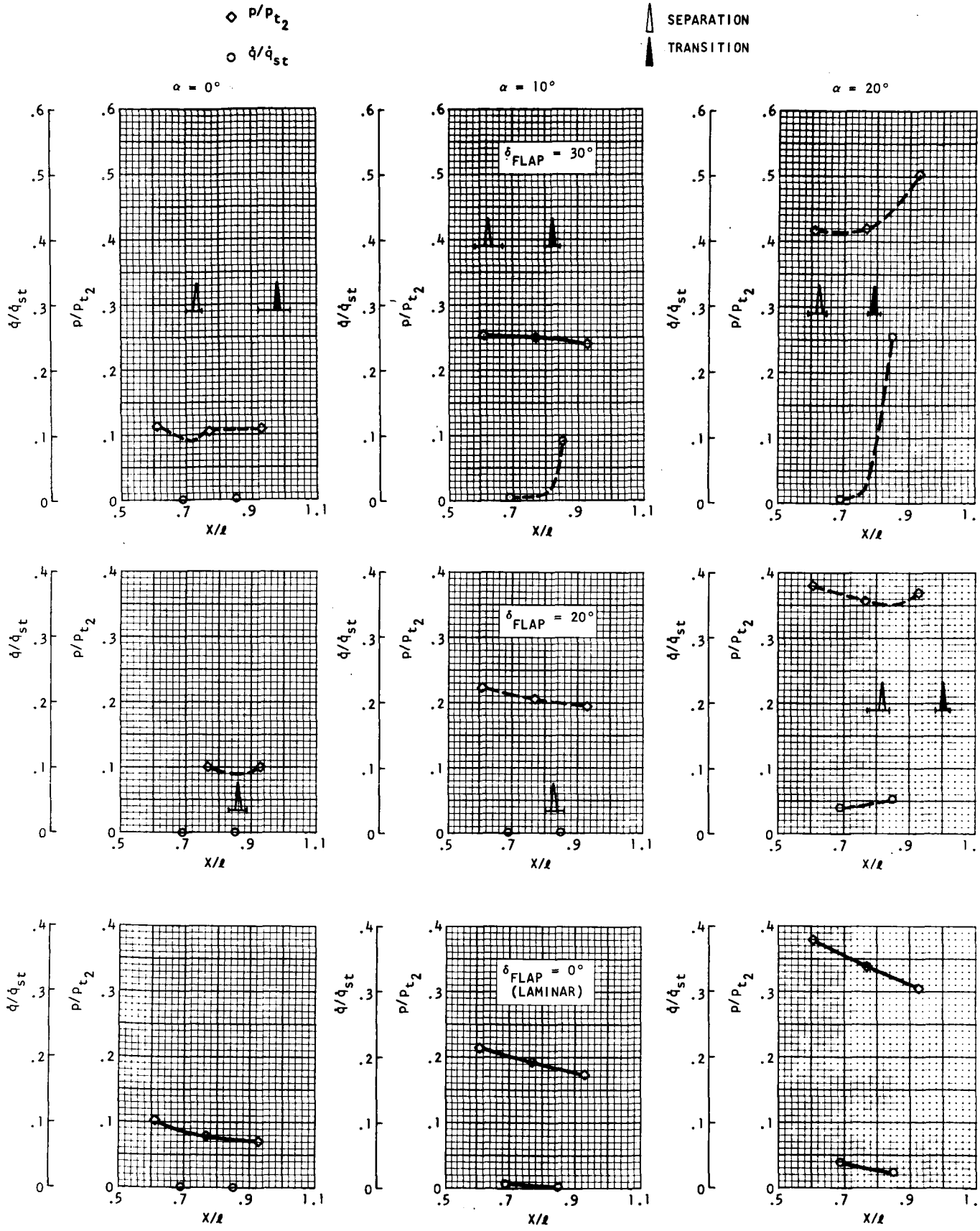

b) R_ℓ = 0.009 TO 0.010

FIGURE 18.--CONTINUED

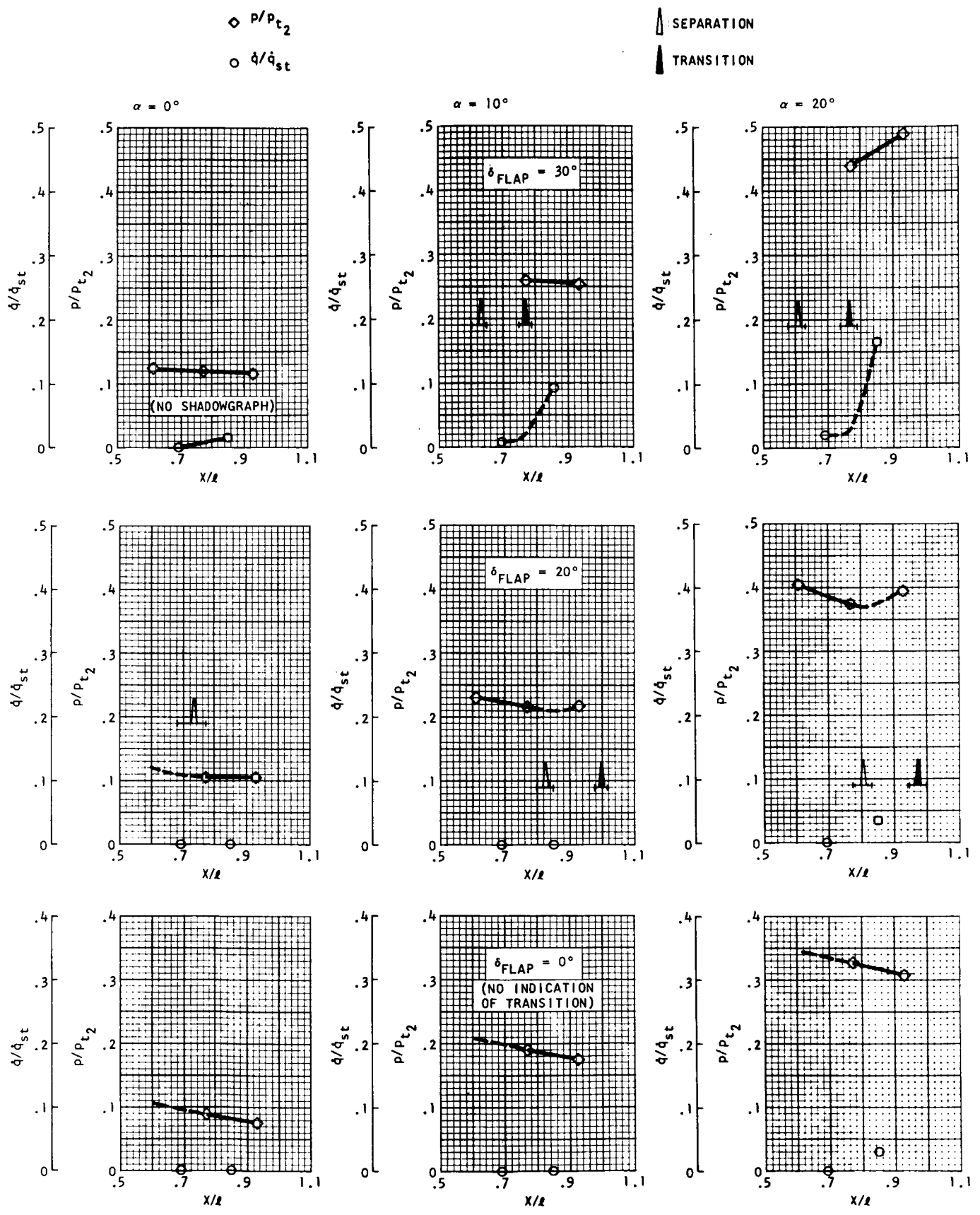

c) α = 0.019 TO 0.022

FIGURE 18.--CONTINUED

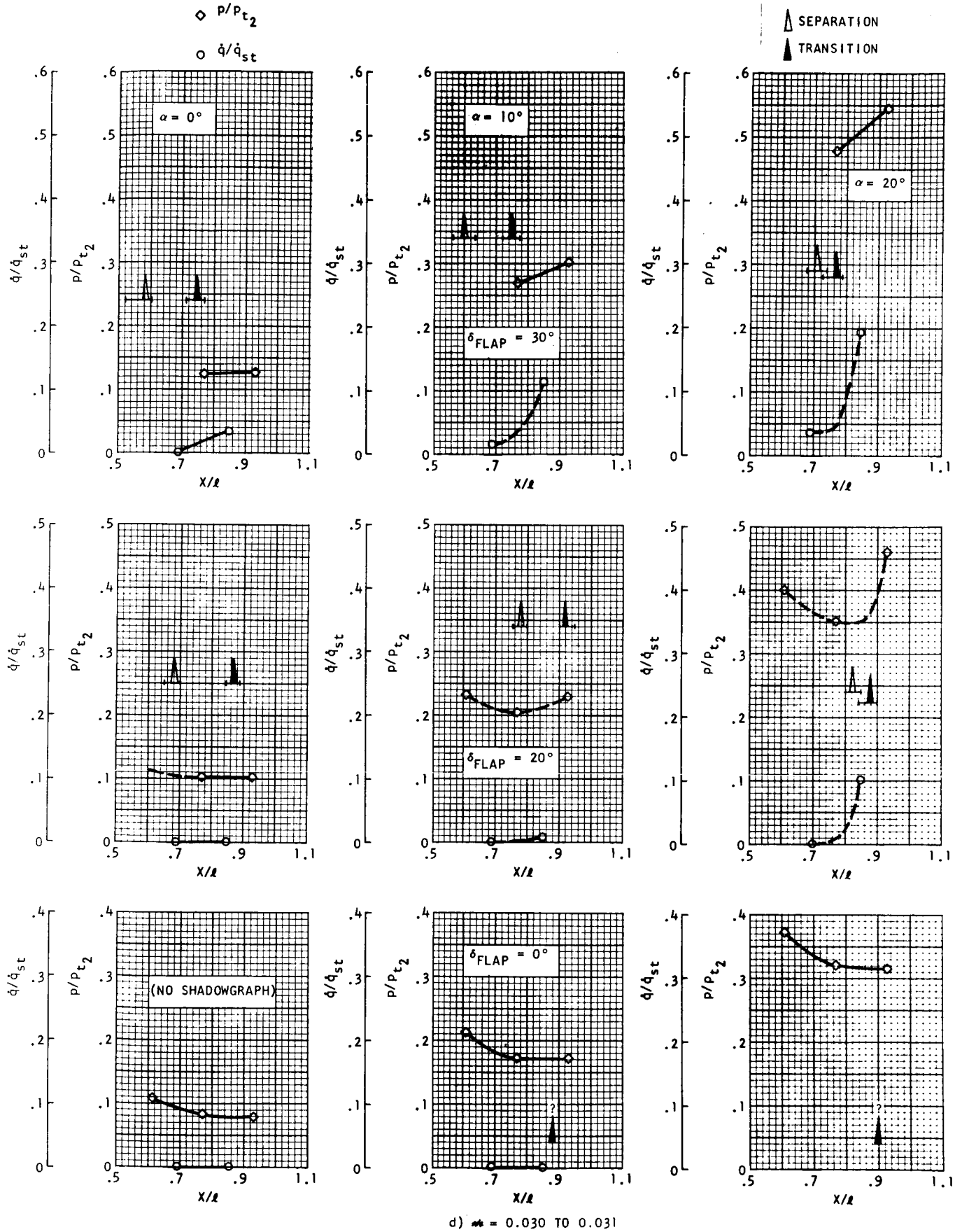

d) m = 0.030 TO 0.031

FIGURE 18.--CONTINUED

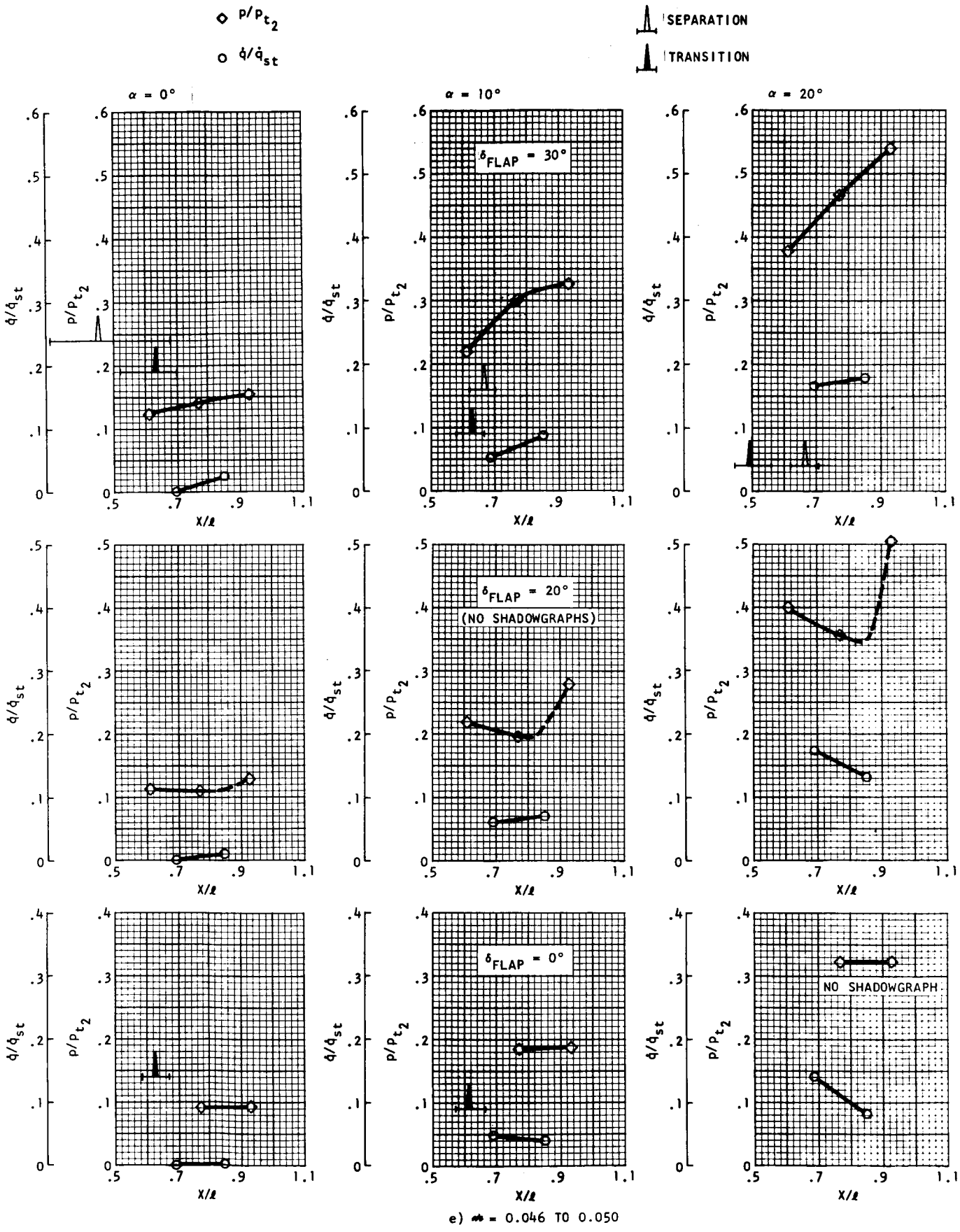

e) $\bar{m}$ = 0.046 TO 0.050

FIGURE 18.--CONCLUDED

little influence on the start of the separation. On the other hand, it is likely that the reattachment line would be sensitive to the total gaseous injection within the separated pocket, which could well be less than in the present experiments. In a purely two-dimensional case, such injection would simply open the pocket so that the so-called dividing streamline would never reattach (ref. 12), though the pressure field associated with the recompression of the stream tubes would be less severely affected. While the separation line in the present three-dimensional case moved little with transpiration rates up to 0.02, the reattachment line on the flap moved steadily rearward, judging by the thermal paint information (figs. 16 and 17) and by the shock wave formation (such as in figs. 6 and 7).

Since the pressures in the nonseparated regions were generally little, if at all, affected by the blowing rates on the present blunt-nosed body, it is this shift in the reattachment line which must be associated with the main changes in the stability and control characteristics of the model. As the reader follows the description of these changes in later discussions, he should keep in mind the preceding discussion of the possible changes in blowing rates within the separated pocket that may occur for different ablators.

Transition to Turbulence in the Separated Layer

Another consequence of the presence of the side sinks and the associated lateral pressure gradients discussed earlier is to bring about three-dimensional shearing of the strong vorticity within the separated layer just upstream of the reattachment. The adverse pressure gradient at reattachment is commonly believed to be rather destabilizing, even without the additional vorticity generation due to the cross-flow. It is therefore not very surprising that transition to turbulence occurs often in this region and, in the past, has tended to confuse the trends of the various aerodynamic quantities with Reynolds number when not carefully observed. While visualization was of great assistance in the present experiments, it cannot be stated positively that fully laminar reattachment was ever present, even though figures (e.g., fig. 6) for zero blowing and $\alpha = 0°$, $\delta = 30°$ would be normally thought as indicating complete laminarity. It can be stated positively that in the present experiments transition invariably occurred for angular combinations $(\alpha + \delta) > 30°$ and $\dot{m} > 0.005$ with $T_w/T_t \approx 0.28$. As blowing or $(\alpha + \delta)$ increased, transition tended to move upstream. When cooling was increased, transition also tended to occur earlier, which is in accordance with Larson's findings (ref. 13) for separated pockets.

Transition is known to be a particularly capricious phenomenon often strongly dependent on the type of disturbances present in the free

stream (especially tunnel side-wall acoustic noise at hypersonic speeds), roughness of the model wall, and presence of three-dimensionality in the boundary layer. It is considerably less capricious in cases where changes in mean boundary layer profiles shift rather rapidly to highly unstable ones such as the onset stages of adverse pressure gradients in the development of separated profiles or in the development of some profiles caused by wall injection, especially when a decreasingly favorable pressure gradient might cease to be sufficiently stabilizing. For such conditions, amplification of the appropriate range of disturbances tends to be exponential in character, almost up to the onset of turbulence. Then the likely near-random ebbing in the magnitude and frequency content of the disturbances results in rather small shifts in the streamwise onset of turbulence (ref. 14).

From the relatively small scatter of the probable instantaneous locations of transition, it would appear that the transition occurring over the separated pocket in the present experiments was generally of the above highly amplified character. The relative Mach number across the developed shear layer was approximately two; still a little low for the high-speed stabilizing trend predicted on theoretical grounds by Lin (ref. 15) and documented experimentally in reference 13 to take full effect. In this respect, flap controlled entry vehicles with rounded noses for which the relative Mach number across the separated layer at the time of the critical heat pulse may be on the order of four or five could be expected to experience the interplay between separation and transition at higher Reynolds numbers and/or higher blowing rates. However, it must be kept in mind that the destabilizing effect of the skew flow upstream of the reattachment was not present in the theoretical and experimental models, which heralded the increase in stability of high-speed shear layers. Caution is indicated with respect to heat transfer at reattachment because the three-dimensional layer, though perhaps laminar, would be especially prone to develop the spanwise unevenness which led to unusually high reattachment heating in Ginoux's experiments (ref. 16).

A larger scatter of instantaneous position of transition appeared to be present in the cases of large blowing (such as in fig. 17a). This composite representation is actually based on five shadowgraphs for which the indicated transition ranged from $x/\ell = 0.52$ to 0.70 (fig. 18e). An even larger motion of transition seemed to occur for the extra cold runs ($T_w/T_t \approx 0.1$), especially with zero flap deflection. While the samples of such runs were too small to warrant general statements, early transition of the attached extra cold boundary layer was observed in these experiments. There could be many explanations for this trend, such as the relative increase in the effective roughness of the combination of the porous-model and possible small-scale uneveness of injection, or locally lingering remnants of frost which was probably occasionally

present. However, since earlier transition with increased cooling has been sporadically reported in specially controlled experiments on very smooth nonpermeable walls (refs. 17, 18 and 19), the present similar trend for a transpired boundary layer is perhaps worth signaling.

Pressure and Heat Transfer Distributions at Standard Temperature

Making sense out of a discrete number of local observations (three pressures and two heat rates when all gages were operating) in presence of complex interacting phenomena presents a problem not unlike that of interpreting flight data. Here, however, the shadowgraph visualization generally provided clear enough indication of the location of separation and transition, the two key observations. Furthermore, the systematic changes in α, δ and $\dot{m}$ make it possible to trace the development of the pressure and heat-flux fields with any of these variables and thus derive additional confidence in the interpretations from the consistency of the various trends. The pressure and heat transfer data thus processed are presented in figures 18a through 18e for the range of injection rates from 0 to 0.05. These displays with α and δ for a given $\dot{m}$, together with indications of probable location of separation and transition (inferred from shadowgraphs, as discussed previously under Optical Technique) are sufficiently consistent to justify joining the discrete data points by solid or dotted lines, the latter indicating a less definite inference. The symbols in the figures represent an average of the local data corrected for small departures of the independent variables α and $\dot{m}$ from the indicated nominal values.

The bottom of figure 18a for zero blowing and zero flap deflection provides a good reference base for the different variations--a base in good agreement with independent hypersonic measurements on a pressure and a heat transfer model of the same shape (figs. 13 and 15). One can trace the nearly proportional rise in $\dot{q}$ and p as the angle of attack increases from 0° to 20° which is expected for laminar boundary layers. The corresponding parts of figures 18b, 18c and 18d demonstrate how effectively the mass injection decreases the heat transfer for laminar boundary layers. (The second gage heat rate of 0.03 at $\alpha = 20°$ in fig. 18c represents one of the few inconsistencies, but the indication of laminarity from the corresponding shadowgraphs is perhaps not positive enough.) In figure 18e, the high injection rates have brought about early transition. Nevertheless, the heat transfer remains significantly less than for the laminar layer without the $\dot{m}$ protection, especially at $\alpha = 0°$ when there was no wall temperature rise in spite of the evident turbulence.

A similar comparison of pressures for $\delta = 0°$ in figures 18a through 18e discloses the relatively small magnitude of indicated pressure changes due to mass injection. These trends are crossplotted in figure 19, and will be discussed later.

As one proceeds to the middle row of figure 18a for $\delta = 20°$, one sees the pressure and heat transfer distributions of the lower row encroached upon by the separation caused by the flap backpressure. As previously mentioned, transition may have been absent, or just incipient, at reattachment for $\delta = 20°$ with $\dot{m} = 0$ and $\dot{m} = 0.01$, $\alpha = 0°$ and $\alpha = 10°$. However, with large injection or larger backpressure $(\alpha + \delta)$, transition moves upstream of the hinge line.

The middle row as well as the case $\delta = 0°$, $\alpha = 20°$ in figure 18e for which there are no shadowgraphs, illustrate the problem of interpretation without visualization. In particular, the change in slope of the heat-transfer distribution might be puzzling. The heat rate normally decreases slowly in the downstream direction for either a laminar or a turbulent layer, and it should drop faster when separation moves past the second heat gage but not the first (e.g., middle row of fig. 18a). The heat rate at the second gage can exceed that at the first rather drastically, when transition moves upstream past the second one but does not reach the first one, such as for $\alpha = 10°$ and $20°$ in the top row of figures 18a through 18d. When transition occurs upstream of separation so that both heat gages are within a turbulent pocket, the rear one may well feel higher heat flux because the bulk of the hot gases would be admitted into the pocket at reattachment. This appears to be the case for the highest blowing rate in the top row of figure 18e. One notes that the turbulent heat flux for higher injection rates ($\dot{m} \geq 0.03$) in or outside the separated pockets (figs. 18d and 18e) never exceeds the laminar flux for no injection, and is substantially less than the turbulent flux for no injection (fig. 18a).

As one flips through figures 18a to 18e one can observe these trends and others--such as the movement of separation and transition with flap angle at all blowing rates. The tendency toward a stabilized separation line, almost independent of $\dot{m}$ and transition, as the pressure gradients build up at higher α and δ values in figure 18 has already been mentioned, as well as the corresponding small variations in pressure level for $\alpha = 20°$ and $\delta = 30°$. The vigorous cross-flows and the sinks at the corners of the flap are probably responsible for this behavior which keeps the controls rather effective.

The exact geometrical and flow conditions at which the various trends above set in are undoubtedly peculiar to the present tests. However, the features of separation, transition, cross-flow and side sinks will be present in designs of most maneuverable entry bodies. One could therefore expect similar interactions between these dominant characteristics but at different, probably higher, Mach and Reynolds numbers.

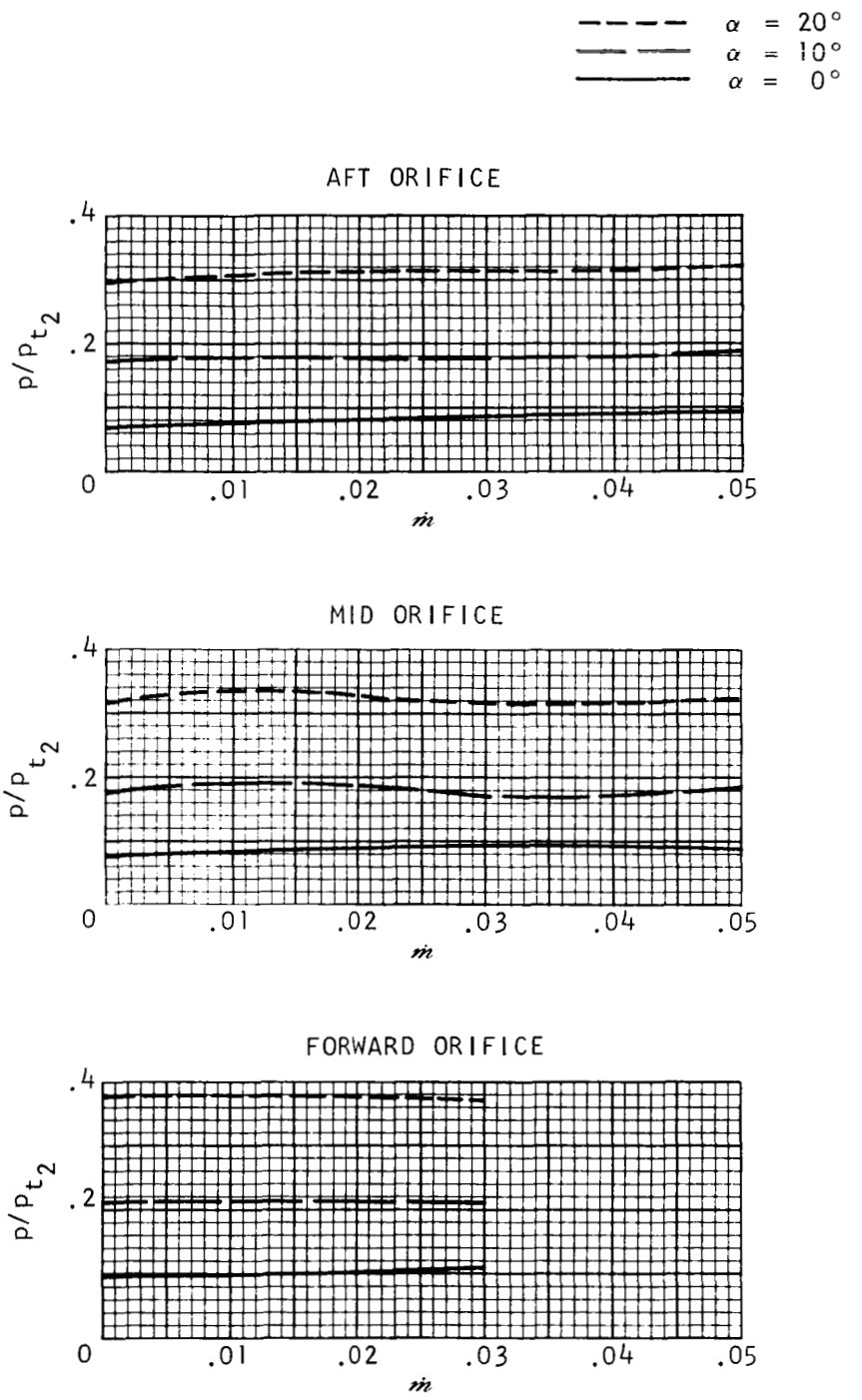

FIGURE 19. PRESSURE RATIO VERSUS m: MACH 7.3, $\delta_{FLAP} = 0°$

The Effect of Cold Nitrogen Injection

The experimental problems multiply rapidly when one attempts to reach in a wind tunnel wall-to-stagnation temperature ratios on the order of 0.1 which are of special practical interest in flight. The early runs were therefore devoted to exploring whether any strong effects of injecting gaseous nitrogen at temperatures as low as 90° K would manifest themselves with 0° and 30° flap deflections. The main effect that emerged was the aforementioned earlier transition which can also be observed in the three heat transfer displays in the right-hand corner of figure 20a for moderate injection rates. Sufficient optical evidence of transition in runs at $\delta = 0°$ corresponding to figure 20a was actually observed only for the medium cooling at $\alpha = 20°$, the image of the boundary layer having been severely deflected into the body silhouette by the high density gradients in the case of coldest injection (bottom row). However, the corresponding heat transfer rates signal unmistakably the occurrence of turbulence, thus corroborating the evidence from neighboring conditions for which the shadowgraphs indicated probable transition. As one would expect, pressure distributions without backpressure were little affected, even by the extreme cooling (fig. 20a).

The effect of cooling in the presence of separated pockets is illustrated for moderate blowing and $\delta = 30°$ in figure 20b. If there are any documentable trends, the slight rearward motion of separation in the second and third row and the rise in pocket pressure at $\alpha = 20°$ may be noticed. One could comfortably rationalize these trends, but much more significant is the absence of any stronger effects so that the bulk of the experiments conducted with the injected mass at room temperatures ($T_w/T_t = 0.28$) acquire additional usefulness.

Effect of Mass Injection for Zero Flap Deflection

The flow and force fields corresponding to the conditions of zero flap deflection at various angles of attack served primarily as bases to which the separated fields caused by increasing flap deflections were compared. As mentioned previously, it was recognized at the outset that a constant total pressure discharge across a porous shell of constant thickness would result in somewhat smaller mass flux near the stagnation point than in the region just upstream of the flap where static pressures are lower (fig. 12). Since separation governed by either a free-interaction law (ref. 1) or dominated by the interplay between pressure gradients and flap backpressures would depend primarily on the local conditions, it was believed that the actual $\dot{m}$ distribution along the boundary would be of secondary importance for a study of control effectiveness. The results support this belief although no adequate characterization of the boundary layers just before separation was obtained.

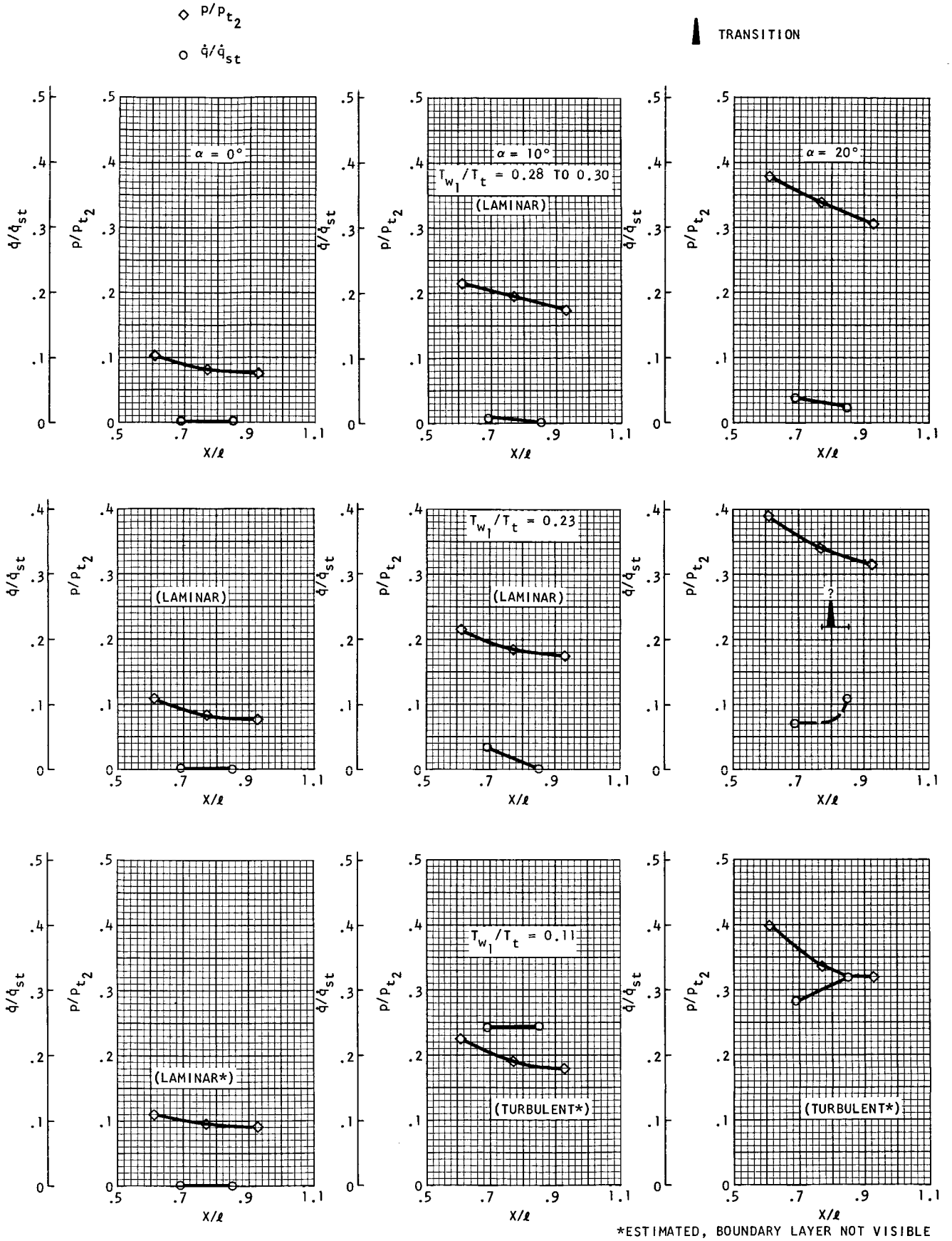

(a) $\dot{m}$ = 0.010 TO 0.012, δ_{FLAP} = 0°

FIGURE 20. PRESSURE AND HEAT RATES AHEAD OF THE FLAP WITH COLD NITROGEN INJECTION: MACH 7.3

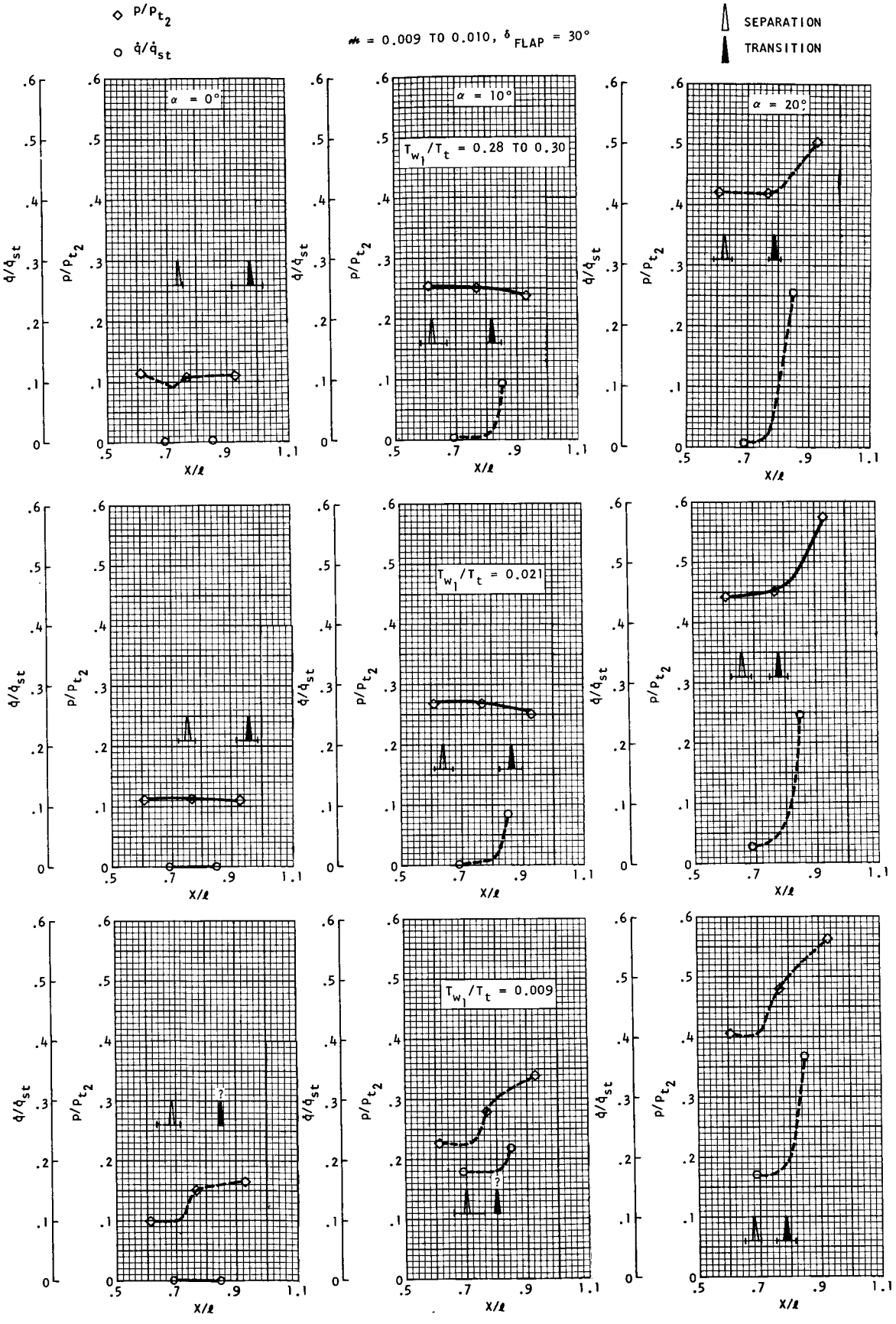

b) $\dot{m}$ = 0.009 TO 0.010, δ_{FLAP} = 0°

FIGURE 20.--CONCLUDED

Since recent measurements of Moore, Stalmach and Pope (ref. 20) and of Bogdonoff (ref. 21) with static pressure orifices located just downstream of the porous areas, exhibited rather large decreases of pressure as $\dot{m}$ was increased, a closer look at the development of the present nonseparated pressure and force fields with $\dot{m}$ was in order. Figure 19 shows that the largest pressure change occurred at the aft orifice for $\alpha = 0°$ (an angle for which cross-flows were minimal), while the changes at the forward orifice were zero within the accuracy of the measurements. Inasmuch as the pressure orifice inserts in the porous metal were identical as far as one could ascertain, the smallness of Δp_{w_1} relative to Δp_{w_3} would indicate that the registered increase in p_{w_3} probably was not due to the disturbance of the local pressure field caused by the presence of the small nonporous plug in the midst of a non-zero normal velocity field. The small undulation of p_{w_2} at the mid-orifice for $\alpha = 10°$ and $20°$ could probably be ascribed to either the vagaries of cross-flows or simply to the inaccuracy of the overall measurements (though the undulation was essentially repeatable). One would then seek an explanation for the cleaner zero angle-of-attack variations of p_{w_1}, p_{w_2} and p_{w_3} in terms of the pressure producing slope of the displacement thickness, $d\delta^*/dx$. On some cold runs, where the shadowgraph contrast is enhanced, a white-black band within the body shadow, similar to that in figure 11 but at the location of p_{w_3}, was observed making an angle with the main body edge in excess of that required for the variation of p_{w_3} ($\dot{m}$). However, in view of the distortion of the light paths discussed earlier, no more than qualitative significance can be attached to these angles.‡

It is very likely that the increase in downstream pressures such as p_{w_3} with $\dot{m}$ would be less for a more realistic distribution $\dot{m}$ (x); i.e., one which would have $\dot{m}$ decrease with p around the body rather than increase slightly as in the present investigation. Since on the blunt nose itself mass injection tends to move the shock layer outward without appreciable change of shape and, therefore, pressure, such a more realistic $\dot{m}$ (x) distribution could be confidently expected to produce a smaller

‡For these cold runs and for $\alpha = 0°$ runs in general, transition at the p_{w_3} location did not appear to be a factor in the observed p_{w_3} variations, judging by optical and heat transfer information.

integrated pressure nose and body effect than encountered here. Thus, it can be surmized that the variation of C_N ($\dot{m}$) and C_m ($\dot{m}$) for zero flap deflection in figures 21 and 22, as small as they are, are probably larger than for a more practical distribution of gaseous injection. The present investigation, properly interpreted, corroborates the view that blunt nose maneuverable bodies (without separated pockets) should experience considerably smaller changes in forces, moments, and stability with $\dot{m}$ than those signalled by Syvertson and McDevitt in their pioneering investigations (refs. 22 and 23) for sharp-nosed cones. The reader can see from figures 21 and 22 that, for $\delta = 0°$, the slopes of C_N and C_m with angle-of-attack decrease in unison by less than eight percent as the blowing rate increases from 0 to 0.05. With a more realistic mass injection distribution, the $\dot{m}$ effect on the stability of blunted maneuverable bodies should become of secondary importance. *

Effect of Mass Injection on Forces and Moments in Presence of Flap Backpressure

Figures 21 and 22 show some decrease in normal force and some deterioration of control effectiveness as mass injection is increased. However, comparisons at constant flap angle disclose no appreciable changes in static stability with $\dot{m}$, a significant result.

The largest relative effects on C_N and C_m occur for $\delta = 30°$ at $\alpha = 0°$ and $10°$. Comparison of the sequence of shadowgraphs for $\delta = 30°$ and $\alpha = 0°$ (figs. 6, 16b, 7 and 17b) together with the pressure variations in the left upper corners of figures 18a through 18e helps one to understand the shift of the pressure field with increasing $\dot{m}$ over the body and flap. Simplified calculations based on measurements inferred from these figures indicate that the integrated incremental pressure force over the flap decreases, while that over the affected body area increases as the rate of mass injection is increased. Since the pitching moment is taken about the center of the base, both these force changes contribute to a positive, nose-up variation approximately of the magnitude depicted in figure 22.

In other words, the deterioration of the control moment at a given δ with blowing appears to correlate with the corresponding enlargement of the pocket, the rearward movement of the reattachment on the flap and the associated pressure changes. In connection with figures 18a through 18e, it was already brought out that as the angle of attack increased, the separated pocket and its pressure tended to become

*Figure 11 of reference 24 (which arrived after this report was completed) corroborates this assessment of changes caused by a more realistic $\dot{m}$ distribution.

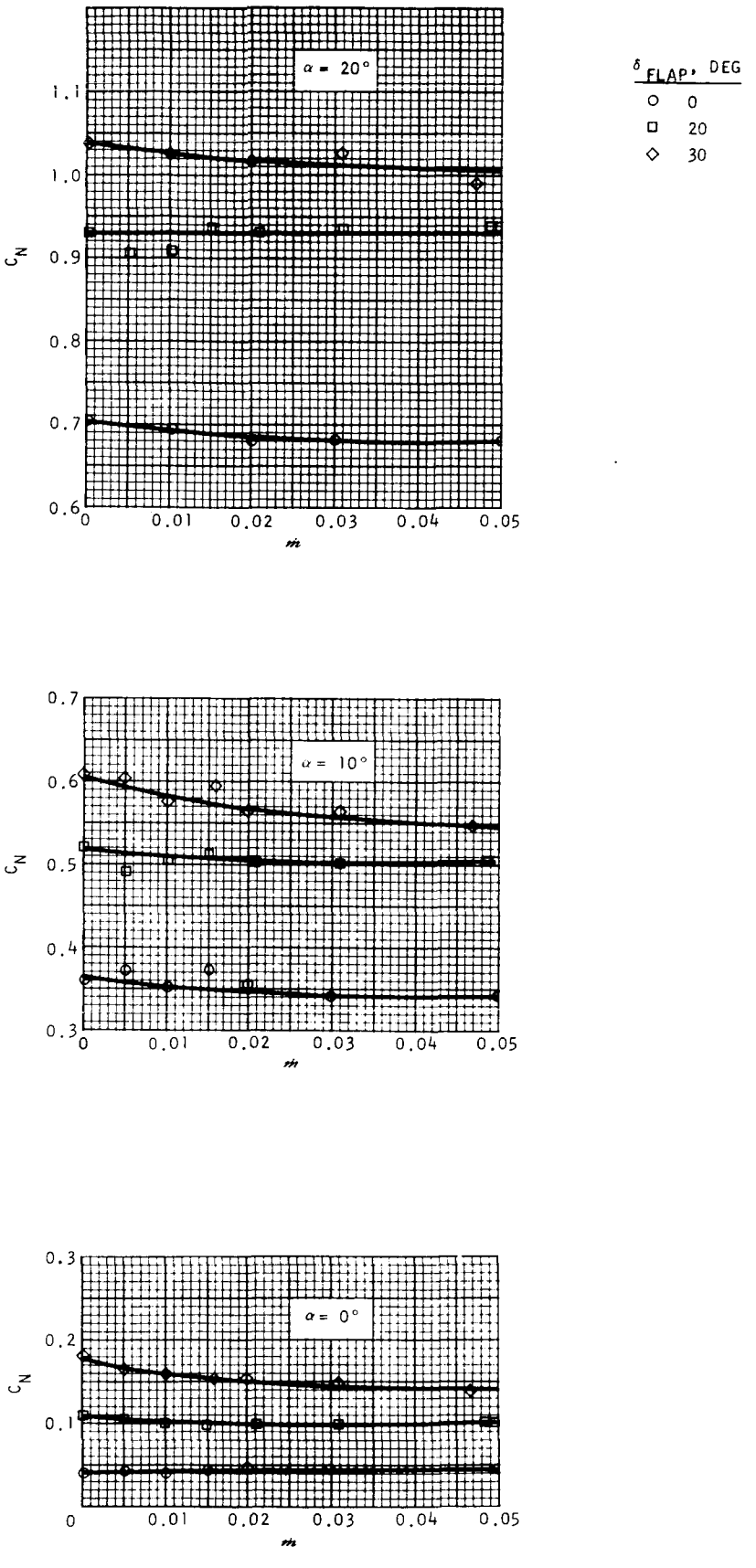

FIGURE 21. C_N VERSUS $\dot{m}$-- ROOM TEMPERATURE NITROGEN: MACH 7.3

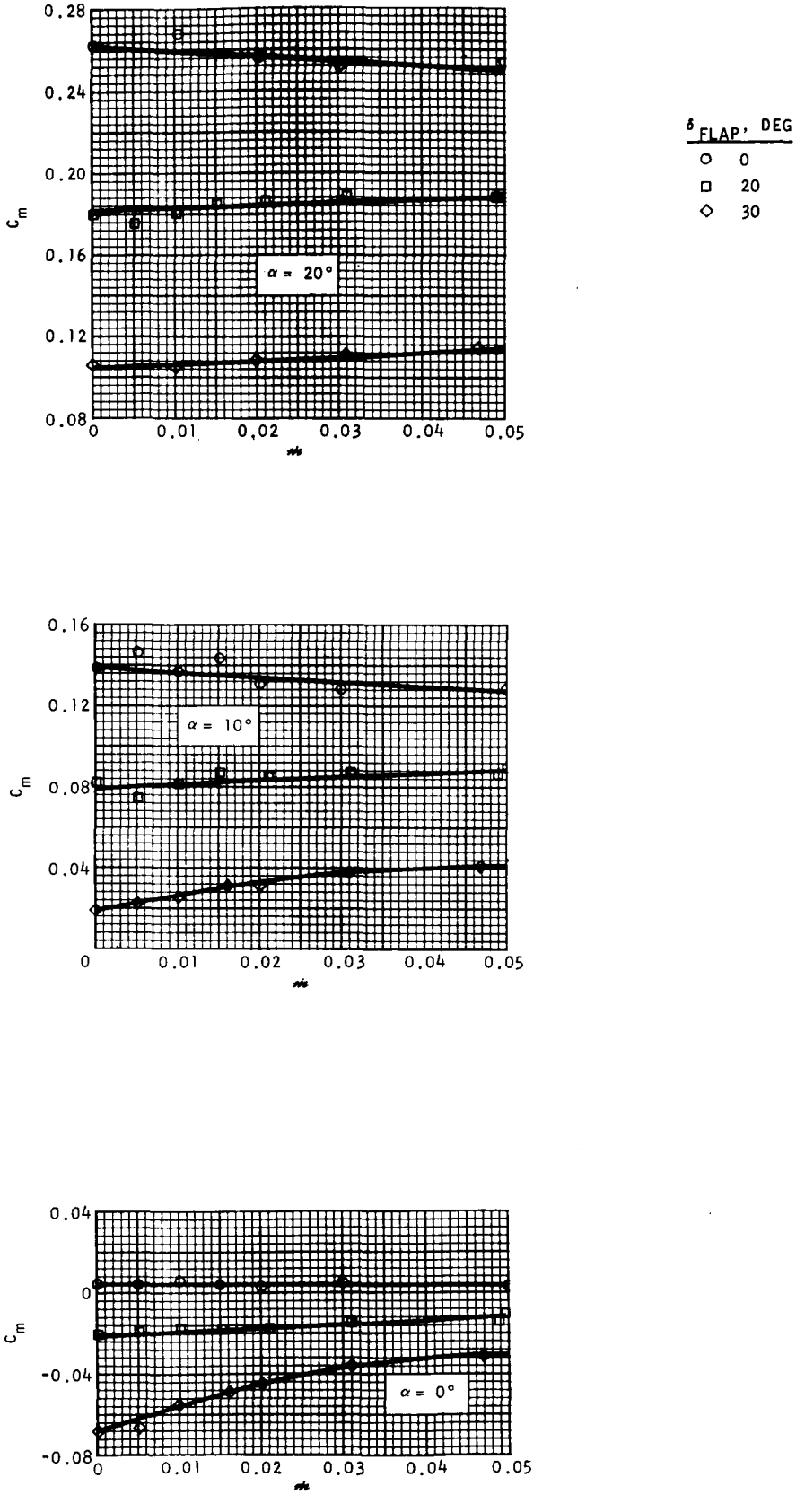

FIGURE 22. C_m VERSUS $\dot{m}$--ROOM TEMPERATURE NITROGEN: MACH 7.3

insensitive to $\dot{m}$. According to the preceding interpretation of the deterioration of C_m at $\alpha = 0°$, the moment and normal force coefficient at $\alpha = 20°$ should also become essentially independent of $\dot{m}$; this, figures 21 and 22 corroborate.

When the changes in C_N are considered, the aforementioned decrease in the net force over the flap at $\alpha = 0°$ is partially compensated for by the increase in the force over the affected body area. In trying to calculate the differences between these effects, one should consider the three-dimensionality of the pressure fields, in particular the probably lower pressures in the areas near the junctures J in figures 16 and 17, where the separated gas funnels outward. Also, in assessing the pressure response at reattachment and downstream of it, one may need to consider the variation of dynamic pressure within the entropy layer (e.g., following the lines of ref. 25). For the purposes of a given maneuverable body prototype, these more elusive effects should be checked by additional pressure distributions over the body and flap, including spanwise variations.

Large Flap Deflections and the Instability of the Separated Pocket

Consider the case of figure 9 when the flap is deflected at the relatively large angle of 51.5° with respect to the free stream direction. Because of the cross-flow, the separation pocket remains small and generates only a weak separation wave, S_S, which barely influences the bow shock, S_B. The upstream influence of the flap is then, for practical purposes, felt up to the flap shock, S_F. The bow and flap shocks combine into the stronger shock ($S_B + S_F$) past their intersection (I), causing a sharp slip surface (SL) across which tangential velocity, density and entropy experience sharp changes. The matching of pressures across SL generally requires that another pressure wave propagates outward from I, in this case an expansion wave, in other cases (such as in fig. 19 of ref. 2) a compression wave. As the angle of the flap increases, this wave (or its equivalent in a more complex interaction such as in fig. 10) will not miss the flap (as in fig. 9), and may in fact fall on the tail segment of the separated surface. In such a case, a possible feedback path upstream through the separated pocket is established and a self-excited motion of the separated pocket may ensue (though other mechanisms are also possible).

Since the bow shock wave wraps more tightly around a body at higher hypersonic speeds, entry vehicles might experience such instabilities for α and δ values encountered during the early part of their trajectory. From ref. 2 and earlier NASA data (refs. 26 and 27), it would appear

that a substantial motion of the effective leading edge of the separated pocket probably forms an important link in the chain of unsteady events. Thus, one can discern a significant upstream shift in separation between the spark shadowgraphs of figures 23a and 23b, taken during the same run upon successive immersions of the present model with zero mass injection. Associated with this shift is a substantial alteration of the merged bow shock-separation shock combination ($S_B + S_S$) and a shift in the position of their intersection (I) and of the upper flap shock (S'_F). (S'_F is a nearly normal shock near I, and its shape is modified by the upper part of the flap through the subsonic region of influence which is bounded by the front face of the flap, shock S'_F and the line in the initial direction of SL.) The instantaneous flow fields in figures 23a and 23b are clearly not repeatable, in particular the location of I with respect to the flap, the shape of SL and the shock S. The latter, in figure 23b, suggests a stage in the evolution of the reattachment flap shock S_F (see figs. 9 and 10 for antecedents). In figure 23a, shock S appears to be almost normal to the local flow so that the tail segment of the separation may be influenced by conditions at I and a feedback loop temporarily closed.

The flap effectiveness, corresponding to figures 23a and 23b, remained high, the increment in C_m between $\delta = 30°$ and $\delta = 60°$ actually exceeding that between $\delta = 0°$ and $\delta = 30°$ by 33 percent (with correction for the change in face area). However, the very high average heat flux and the unsteady loads on the flap would probably make such conditions undesirable in flight.

There is concern that, in the presence of mass injection in flight (ablation) with the consequent lower than normal shear stress at the wall, the boundary layer would become much more susceptible to separation and, hence, to the above type of unsteady flows, possibly even at lower deflection angles.

Limited experiments at flap angles of 40° and 60° at maximal (presumably more critical) blowing rates between 0.047 and 0.051 disclosed no additional adverse effects due to $\dot{m}$. Figures like 23c and 23d appear no more critical than figures 23a and 23b for zero injection. If anything, the location of the intersection I with respect to the flap is farther outward for $\dot{m} = 0.05$, an indication of lesser danger of instabilities. There was unsteadiness (less so for $\delta = 40°$), but no susceptibility to motion of the leading edge of separation due to $\dot{m}$ was evident. Such behavior would be consistent with the previous observations that, for sufficiently large favorable pressure gradients (at least for the present three-dimensional model), the separation phenomenon appeared affected little by mass addition at the wall.

In the present experiments, protrusion of the flap through the bow shock S_B (characterized by the motion of the intersection I to a level

below the tip of the flap and by the appearance of S'_F) was not quite coincident with the appearance of the unsteadiness of the separated pocket. However, such protrusion did coincide with rapid increase in the slope of C_m with α. The case of $\alpha = 10°$, $\delta = 40°$ illustrated rather dramatically that large mass injection can postpone the protrusion somewhat. For $\dot{m} = 0.05$, the intersection I was above the flap tip, while C_m had the value of -0.017. For $\dot{m} = 0$, the intersection I moved in front of the flap and C_m increased to -0.058. For a narrow range of α and δ values (within which $\alpha = 10°$, $\delta = 40°$ happen to fall in the present experiments), mass injection may actually postpone unsteadiness as well.

Some Design-Oriented Observations

The degree of consistency in the finite flap separation phenomenon with mass injection in the present experiments (even for high flap deflections) is sufficiently encouraging to attempt to draw some more general qualitative guidelines. It appears that, for blunted maneuverable bodies operating at moderate L/D ratios, the extent of upstream separation may be largely dominated by the local favorable pressure gradients and by the geometry of the flap (which controls the location of the side sinks and sets the level of the backpressure), rather than by the gaseous mass injection and the characteristics of the boundary layer. Thus, for flap deflections between 20° and 30° and angles of attack between 10° and 20° (the approximate operating region if the present model shape were to be used), the separation leading edge and the pressures upstream of the flap were only mildly sensitive to the degree of blowing. Also, the differences between cases where the separation was turbulent and those where the layer separated laminarily were rather small, perhaps because transition generally took place shortly after separation.

An entry vehicle for which the shape of the separation pocket over the body is stabilized by such pressure-geometry interaction should not experience any catastrophic deterioration of control effectiveness because of increasing rates of ablation. However, vehicles with flatter geometries and nearly constant pressure distributions (with x), such as sharp cones at small angles of attack and some contemplated high L/D shapes, may well be sensitive to $\dot{m}$. For such cases, a given back pressure may propagate substantially larger distances upstream as mass injection modifies the balance between skin friction and the local pressure rise required for separation. No generalization concerning the mild decrease in control effectiveness for such vehicles should be made on the basis of the present experience. However, the deliberate utilization in design of local shaping of the vehicle to bring about local favorable pressure gradients in order to limit the forward spread of separation is suggested by the present experiments.

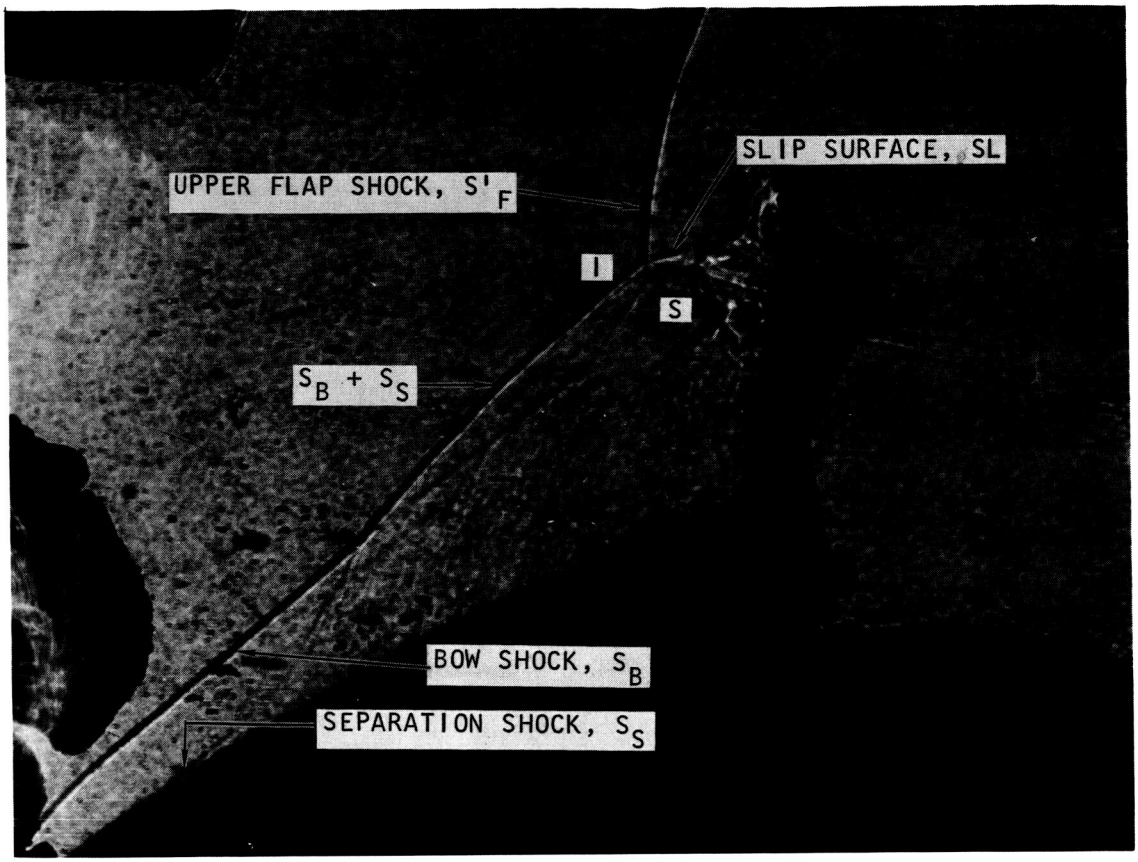

(a)

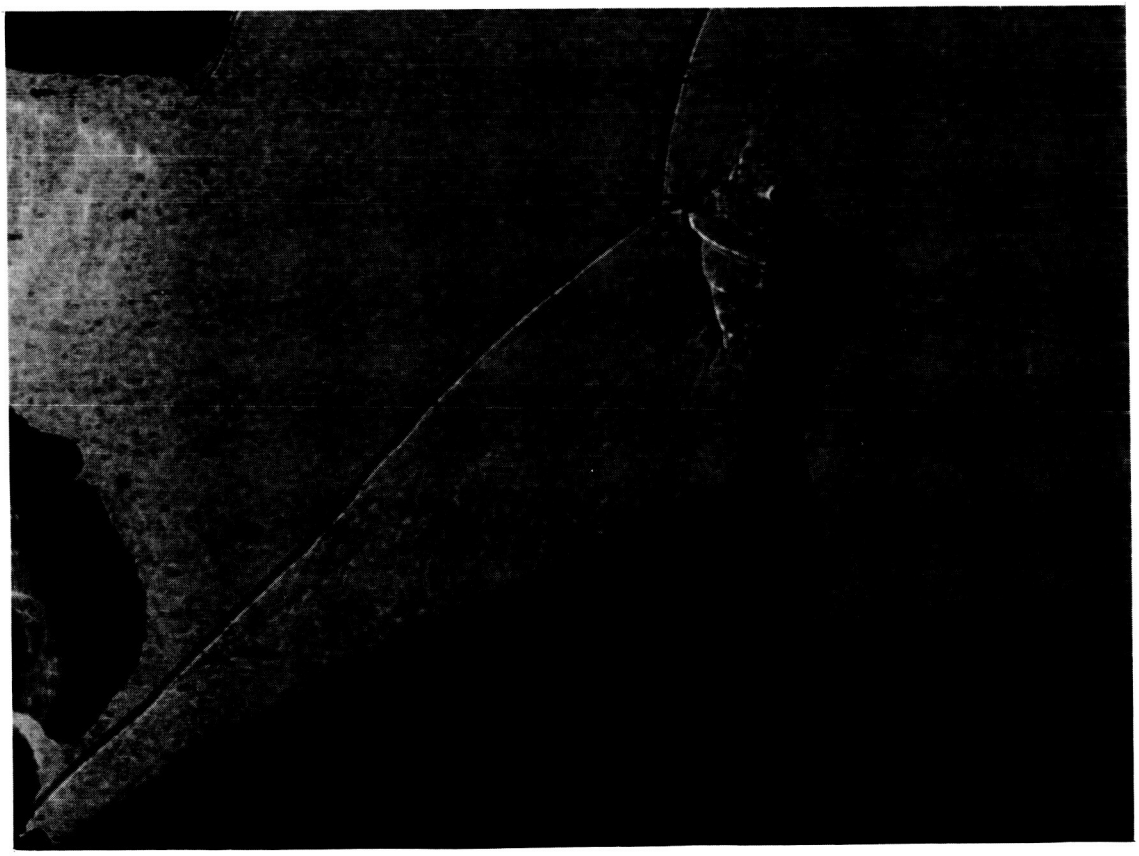

(b)

FIGURE 23. SHADOWGRAPHS: FLAP AT 60°

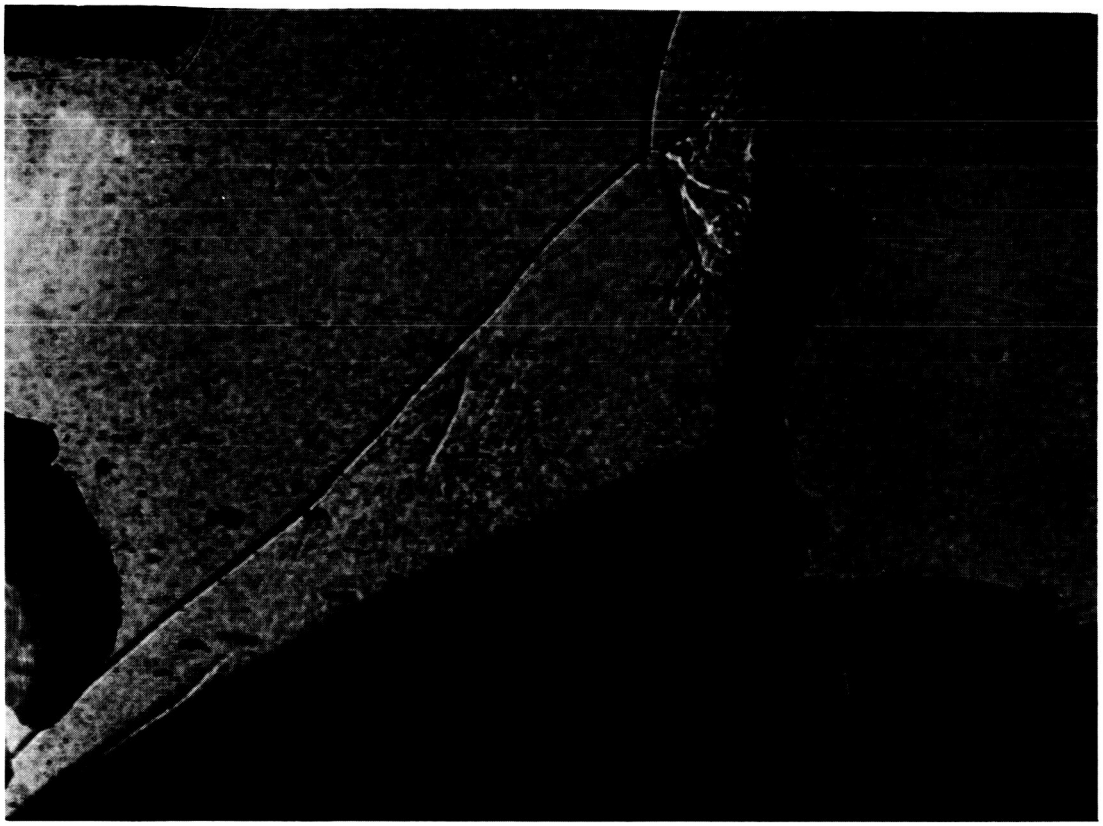

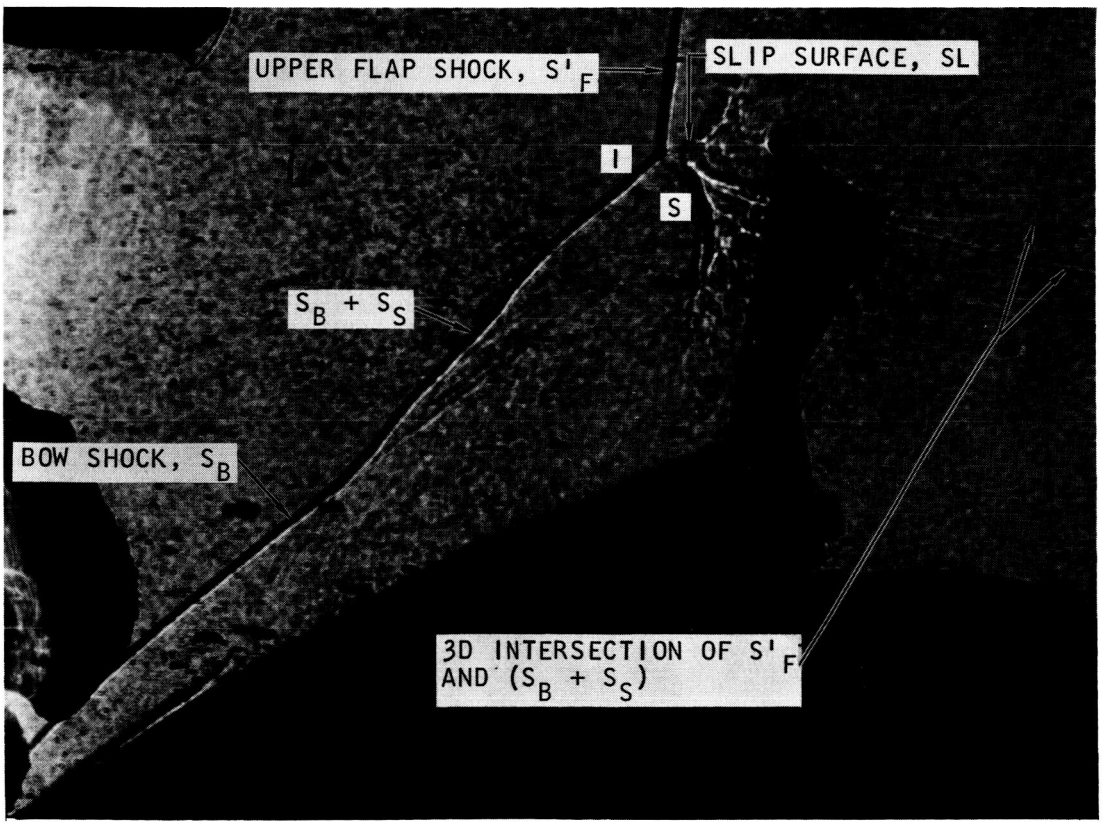

(d)

FIGURE 23.--CONCLUDED

Even for blunted shapes there is some deterioration of control effectiveness with $\dot{m}$, especially at lower angles of attack, when the favorable pressure gradients are reduced. Part of this effect is due to the rearward motion of the reattachment line and the consequent pressure distribution shift over the flap. The scaling of this last effect with Reynolds number and $\dot{m}$ remains an open question.

A remark is in order concerning the role of the aspect ratio of the control surface. While low aspect ratio often connotes poor effectiveness, it should be remembered that, at high speeds, a low aspect ratio also brings the side sinks (near junctures J in figs. 16 and 17) closer together, and thereby limits sharply the size of the separated pocket. This effect maintains control effectiveness, even in presence of large $\dot{m}$ values.

The lack of sensitivity to $\dot{m}$ in the present experiments reinforces the conjecture that separation and control effectiveness are rather independent of the streamwise distribution of $\dot{m}$ (x). Therefore, the fact that the single stagnation chamber within the porous shell of constant thickness yields somewhat unrealistic $\dot{m}$ (x) distribution is not considered to be significant as far as control effectiveness is concerned.

The cohesive link between the often peculiar trends of p(x) and $\dot{q}$(x) in figure 18 was provided by the visual information from the shadowgraphs, which called for the relatively high density and, therefore, unit Reynolds number of the present experiments. As noted earlier, it is possible that the lack of sensitivity of the separated pocket at $\alpha \geq 10°$ is associated with the fact that transition of the separated layer followed separation rather closely. The point has been made that both the adverse pressure gradient near reattachment at flap deflection $\delta \geq 20°$ and the lateral pressure gradients due to the finiteness of the flap and the consequent skew shear flow in the separated layer are likely to bring about early transition. However, at higher Mach numbers and lower Reynolds numbers, the separated layer may possibly be stable enough that an essentially laminar behavior may govern. For such cases, the present experiments offer few guidelines. A comparable investigation of $\dot{m}$ effects for such cases is probably in order, hampered as it may be by the lack of visualization aid. However, even for such cases of laminar separation and laminar reattachment, the pocket shape and size should be expected to be strongly influenced by the outflow at the junctures J of figures 16 and 17, and by the pressure gradient-back-pressure interplay which dominated the present experiments with turbulent reattachment at moderate and high angular settings of α and δ.

CONCLUSIONS AND RECOMMENDATIONS

An exploratory investigation of the effect of wall mass injection on the forces, moments, stability and control characteristics of a blunt-nosed entry model was conducted at Mach number 7.3 in the NASA Ames 3.5-foot Hypersonic Wind Tunnel. Special attention was paid to the separation characteristics of the mass-augmented boundary layer by taking extensive spark shadowgraphs and by monitoring discrete sets of pressures, temperatures and heat-flux rates at the surface of the porous sintered-steel model just upstream of the 1.6 aspect-ratio trailing edge flap. The mass rate parameter (the ratio of total injected mass to the product of free stream velocity, density and body base area) was varied over the practically important range between 0 and 0.05. Inferences made from the resulting data were:

(1) The effect of gaseous emanation from the surface on the external aerodynamics of blunt-nosed bodies with zero flap deflection is substantially less than for sharp bodies with the same base area (figs. 19, 21 and 22 for $\delta = 0°$).

(2) Local flow fields associated with a small aspect ratio flap placed in an otherwise favorable pressure gradient appear governed by the powerful venting of the separated pocket at the junctures of the flap with the trailing edge, by the magnitude of the pressure gradient, and by the backpressure which the flap can propagate through the separated pocket. As the favorable pressure gradient increases, the size of the separated pocket tends to become insensitive to the rate of mass injection at the wall. Consequently, the normal force coefficient and the moment coefficient depend only mildly on blowing, especially as angle of attack increases. At lower angles of attack there is some deterioration of flap effectiveness but not of stability (dC_m/dC_N) with blowing (figs. 21 and 22).

(3) At a Reynolds number (based on length) of approximately 0.48 million, the lateral and adverse pressure gradients existing upstream of reattachment appear strongly destabilizing, so that flap deflections higher than 20° invariably effect transition to turbulence in the separated skewed shear layer. It is recommended that more attention be paid to the probability of shear layer destabilization by lateral pressure gradients which are usually present in practical configurations with separated flow. It is also recommended that an investigation similar to the present one be conducted at higher Mach numbers and lower Reynolds numbers, even though visualization will probably be lost, so that the behavior described in (2) could be verified for an essentially laminar pocket.

(4) The major effect of decreasing the ratio of the wall temperature to the stagnation temperature from 0.28 to below 0.1 was to effect earlier transition in both the attached layers at zero flap deflection and in the

separated layers for finite flap deflections. The measured pressures and forces appeared almost insensitive to such wall cooling to the accuracy of the experiments. This is consistent with (2), and increases the usefulness of the bulk of the experiments which were conducted with the surface temperatures at room level.

(5) As flap deflections and/or angles of attack of the blunt-nosed body increase, the flap protrudes from behind the bow shock wave and, at somewhat higher angles, a large-scale unsteadiness of the separated pocket sets in. A limited sample of such conditions at flap angles of 30°, 40° and 60° indicates that mass injection is not likely to aggravate the unsteadiness, contrary to earlier conjectures. Since such conjectures were based on the assumption that variation in local skin friction would have a prominent role in determining the separation pocket, these indications again tend to confirm (2). In fact, at very high injection rates, there was evidence that the onset of unsteadiness may be delayed.

(6) Throughout the experiments, the mass injection was very effective in keeping the local heat flux rates down for attached or separated, laminar or turbulent boundary layers over the body (fig. 18). Judging by the behavior of thermal paints, the flap (not protected by local mass injection) enjoyed substantial protection from the upstream injection, even for highly turbulent conditions.

REFERENCES

1. Chapman, D. R.; Kuehn, D. M.; and Larson, H. K.: Investigations of Separated Flows in Supersonic and Subsonic Streams with Emphasis on the Effect of Transition. NACA Rept. 1356, 1958 (Supersedes NACA TN 3869).

2. Goldman, R. L.; Morkovin, M. V.; and Schumacher, R. N.: Unsteady Control Surface Loads of Lifting Re-entry Vehicles at Very High Speeds. Preprint 67-15, Am. Inst. Aeron. and Astronaut., January 1967.

3. Sterrett, J. R.; and Emery, J. C.: Extension of Boundary-Layer-Separation Criteria to Mach Number of 6.5 by Utilizing Flat Plates with Forward-Facing Steps. NASA TN D-618, 1960.

4. Holder, D. W.; North, R. J.; and Wood, G. P.: Optical Methods for Examining the Flow in High-Speed Wind Tunnel. AGARDograph 23, 1956.

5. Jedlicka, J. R.; Wilkins, M. E.; and Seiff, A.: Experimental Determination of Boundary-Layer Transition on a Body of Revolution at M = 3.5. NACA TN 3342, 1954.

6. Seiff, A.; Sommer, S. C.; and Canning, T. N.: Some Experiments at High Supersonic Speeds on the Aerodynamic and Boundary-Layer Transition Characteristics of High-Drag Bodies of Revolution. NACA RM A56I05, 1957, Declassified May 1961.

7. Equations, Tables and Charts for Compressible Flow. NACA Rept. 1135, 1953.

8. Fay, J. A.; and Riddell, F. R.: Theory of Stagnation Point Heat Transfer in Dissociated Air. J. Aeron. Sci., vol. 25, no. 2, Feb. 1958, pp. 73-85.

9. Separated Flows. Vol. I and II, AGARD Conf. Proc. No. 4 (Proc. of Specialists Meeting on Separated Flows held in Rhode-Saint-Genese, Belgium 10-13 May 1966), Discussion in AGARD Rept. 526, 1967.

10. Stern, I.; and Rowe, W. H.: Effect of Gap Size on Pressure and Heating over the Flap of a Blunt Delta Wing in Hypersonic Flow. Preprint 66-408, Am. Inst. Aeron. and Astronaut., 1966.

11. Larson, Howard K.: Heat Transfer in Separated Flows. J. Aerospace Sci., vol. 26, no. 11, Nov. 1959, pp. 731-738.

12. Nicoll, Kenneth M.: Mass Injection in a Hypersonic Cavity Flow. Gas Dynamics Laboratory Rept. 714, Princeton University Dept. of Aeron. Engineering, Dec. 1964.

13. Larson, Howard K.; and Keating, Stephen J.: Transition Reynolds Numbers of Separated Flows at Supersonic Speeds. NASA TN D-349, 1960.

14. Smith, A. M. O.: Transition, Pressure gradient, and Stability Theory. Proceedings of the Ninth International Congress of Applied Mechanics, vol. 4, pp. 234-244, 1957.

15. Lin, C. C.: On the Stability of the Laminar Mixing Region Between Two Parallel Streams in a Gas. NACA TN 2887, 1953.

16. Ginoux, J. J.: Streamwise Vortices in Laminar Flow. AGARDograph No. 97, 1965, Proc. Symposium on Boundary Layers held in Naples, May 1965, pp. 397-422.

17. Jack, J. R.; Wisniewski, R. J.; and Diaconis, N. S.: Effects of Extreme Surface Cooling on Boundary Layer Transition. NACA TN 4094, 1957, also J. Aerospace Sci., vol. 28, p. 1950, 1961.

18. Sheetz, N. W.: Free-Flight Boundary - Layer Transition Investigations at Hypersonic Speeds. Preprint 65-127, Am. Inst. Aero and Astronaut., Jan. 1965, also J. Aerospace Sci., vol. 29, p. 352, May 1962.

19. Richards, B. E.; and Stollery, J. L.: Transition Reversal on a Flat Plate at Hypersonic Speeds. AGARDograph 97, pp. 483-501, May 1965.

20. Moore, D. R.; Stalmach, C. J.; and Pope, T. C.: Investigation of Ablation Effects on Hypersonic Dynamic Stability of a 10° Cone. Air Force Flight Dyn. Lab., AFFDL-TR-66-230, Jan. 1967.

21. Bogdonoff, S. M.: Research on Hypersonic Flow. USAF, Office of Aerospace Research, ARL 67-0009. Jan. 1967.

22. Syvertson, C. A.; and McDevitt, J. B.: Effects of Mass Transfer Cooling on the Static Stability and Dynamic Motions of Slender Entry Vehicles. Transactions of the 8th Symposium on Ballistic Missiles and Space Technology, 16-18 October 1963.

23. Syvertson, C. A.; and McDevitt, J. B.: Effects of Mass Addition on the Stability of Slender Cones at Hypersonic Speeds. J. Aerospace Sci., vol. 1, no. 4, April 1963.

24. Jorgensen, Leland H.; and Hagen, Jack R.: Measured and Computed Static Aerodynamic Characteristics of Ablating Conical Teflon Models at Mach Number 14. NASA TN D-4022, June 1967.

25. Seiff, A.; and Whiting, E. E.: Calculation of Flow Fields from Bow-Wave Profiles for the Downstream Region of Blunt-Nosed Circular Cylinders in Axial Hypersonic Flight. NASA TN D-1147, Nov. 1961.

26. Holdaway, George H.; Polek, Thomas E.; and Kemp, Joseph H.: Aerodynamic Characteristics of a Blunt Half-Cone Entry Configuration at Mach Numbers of 5.2, 7.4, and 10.4. NASA TM X-782, Jan. 1963.

27. Kemp, Joseph H.; Holdaway, George H.; and Polek, Thomas E.: Characteristics of an Aerodynamic Control System for Use with Blunt Entry Configurations at Mach Numbers of 10.7 and 21.2 in Helium. NASA TM X-1153, Oct. 1965.